MEDICAL TECHNOLOGY

An electroencephalogram microdisplay to visualize neuronal activity on the brain surface

Youngbin Tchoe[1,2]†, Tianhai Wu[1]†, Hoi Sang U[1], David M. Roth[1,3], Dongwoo Kim[1], Jihwan Lee[1], Daniel R. Cleary[1,4,5], Patricia Pizarro[1,6], Karen J. Tonsfeldt[1,7], Keundong Lee[1], Po Chun Chen[1], Andrew M. Bourhis[1], Ian Galton[8], Brian Coughlin[9,10], Jimmy C. Yang[11,12], Angelique C. Paulk[9,10], Eric Halgren[5], Sydney S. Cash[9,10], Shadi A. Dayeh[1,13]*

Functional mapping during brain surgery is applied to define brain areas that control critical functions and cannot be removed. Currently, these procedures rely on verbal interactions between the neurosurgeon and electrophysiologist, which can be time-consuming. In addition, the electrode grids that are used to measure brain activity and to identify the boundaries of pathological versus functional brain regions have low resolution and limited conformity to the brain surface. Here, we present the development of an intracranial electroencephalogram (iEEG)–microdisplay that consists of freestanding arrays of 2048 GaN light-emitting diodes laminated on the back of micro-electrocorticography electrode grids. With a series of proof-of-concept experiments in rats and pigs, we demonstrate that these iEEG-microdisplays allowed us to perform real-time iEEG recordings and display cortical activities by spatially corresponding light patterns on the surface of the brain in the surgical field. Furthermore, iEEG-microdisplays allowed us to identify and display cortical landmarks and pathological activities from rat and pig models. Using a dual-color iEEG-microdisplay, we demonstrated coregistration of the functional cortical boundaries with one color and displayed the evolution of electrical potentials associated with epileptiform activity with another color. The iEEG-microdisplay holds promise to facilitate monitoring of pathological brain activity in clinical settings.

INTRODUCTION

The goal of neurosurgical treatment is complete resection of pathologic tissue. However, there is usually a trade-off between the extent of resection and the risk of postoperative neurological deficit due to loss of functional tissue (*1–6*). Because brain lesions can distort normal anatomy and cause functional reorganization (*7*) that may not be fully identified with noninvasive functional neuroimaging techniques, direct electrical stimulation (DES) paired with electrophysiological recording has evolved as the gold standard for determining functional boundaries before resection of lesions located in eloquent areas (*8–12*). DES is a reliable, safe, and effective technique for the identification and preservation of cortical and subcortical neuronal pathways for motor, sensory, language, and memory function (*8, 12*). More recently, passive electrophysiological recordings in the high gamma band (60 to 200 Hz) were shown to be a fast, robust, and reliable method for identifying receptive language areas (*13*) with differences in brain activity entropy and high gamma activity (HGA) characterizing pathological tissue in brain tumors (*3, 14, 15*). On the basis of DES mapping, functional regions are marked and preserved from resection, usually with a margin of about 5 mm around the motor areas and 7 mm around the language areas to avoid postoperative functional deficit (*16*). Most commonly, identifying the spatial extent of functional and pathological boundaries based on neurophysiology is communicated verbally by messages written on paper that are transported across the operating room between the intraoperative monitoring team composed of clinical electrophysiologists, neurologists, and the neurosurgeons. Moreover, some groups use sterile paper placed on the surface of the brain to mark areas for resection and areas for preservation (*8, 17*). The resolution and the methodology for presenting this critical information to guide neurosurgical interventions can be improved.

Recent advances in thin-film microelectrode technology have increased the resolution by which cortical activity can be measured and localized (*18–20*). For example, platinum nanorod grids (PtNRGrids) have been used to identify the curvilinear boundary between functional and pathological tissues in the human brain at unprecedented spatial resolution (*20*). However, to date, there is no available technology that can display these cortical boundaries in situ on the brain. The rise of flexible panel display technology presents an opportunity to revolutionize the way we measure and display cortical activity. In the display technology field, gallium nitride (GaN) light-emitting diodes (LEDs) represent an efficient and scalable solution for solid-state lighting and displays (*21*) and have recently progressed to full-color capability with layer-transfer techniques of micro-LEDs (μLEDs) (*22*). However, the monolithic integration, encapsulation, and release of freestanding GaN μLED arrays from wafers suitable for production scale with diameters exceeding 15.24 cm have not been previously accomplished.

To address the need for high-fidelity, real-time tracking of functional and pathological brain activity and to advance the use of GaN μLED display tools, here, we describe a fabrication procedure for

[1]Integrated Electronics and Biointerfaces Laboratory, Department of Electrical and Computer Engineering, University of California, San Diego, La Jolla, CA 92093, USA. [2]Department of Biomedical Engineering, Ulsan National Institute of Science and Technology, Ulsan 44919, Korea. [3]Department of Anesthesiology, University of California, San Diego, La Jolla, CA 92093, USA. [4]Center for the Future of Surgery, Department of Surgery, University of California, San Diego, La Jolla, CA 92093, USA. [5]Department of Neurological Surgery, University of California, San Diego, La Jolla, CA 92093, USA. [6]Department of Neurological Surgery, Oregon Health & Science University, Mail code CH8N, 3303 SW Bond Avenue, Portland, OR 97239, USA. [7]Department of Obstetrics, Gynecology, and Reproductive Sciences, Center for Reproductive Science and Medicine, University of California, San Diego, La Jolla, CA 92093, USA. [8]Department of Electrical and Computer Engineering, University of California, San Diego, La Jolla, CA 92093, USA. [9]Department of Neurology, Center for Neurotechnology and Neurorecovery, Massachusetts General Hospital, Boston, MA 02114, USA. [10]Department of Neurology, Harvard Medical School, Boston, MA 02115, USA. [11]Department of Neurosurgery, Massachusetts General Hospital, Boston, MA 02114, USA. [12]Department of Neurological Surgery, Ohio State University, Columbus, OH 43210, USA. [13]Departments of Radiology and Neurosciences, University of California, San Diego, La Jolla, CA 92093, USA.
*Corresponding author. Email: sdayeh@ucsd.edu
†These authors contributed equally to this work.

flexible GaN μLEDs and the application of this innovation to a flexible brain electroencephalogram microdisplay (iEEG-microdisplay). The iEEG-microdisplay comprises GaN μLEDs mounted behind the PtNRGrids and acquisition and control electronics and software drivers to analyze and project the cortical activity directly from the surface of the brain. We demonstrated the safe and effective use of the iEEG-microdisplay through benchtop characterization. Moreover, we demonstrated that highly localized brain activity could be projected through the light display in the iEEG-microdisplay in experiments in rats and pigs. In the pig model, we demonstrate that the iEEG-microdisplay provided automated and real-time visual representation of somatosensory evoked potentials (SSEPs). In addition, large voltage deflections correlated with epileptic discharges were coregistered to mapped sensory regions using a dual-color iEEG-microdisplay. In the rat model, we show that the iEEG-microdisplay resolved and represented individual cortical columns and displayed pathological activity with high definition. The combination of PtNRGrids, which allow detection of fine resection boundaries in human brains (20), with iEEG-microdisplays that display cortical activities with spatially corresponding light patterns might help to advance neurosurgical procedures.

RESULTS

iEEG-microdisplay development

To construct the iEEG-microdisplay, we combined ultrathin PtNRGrids previously used for micro-electrocorticography (μECoG) (20) with GaN μLEDs. We chose GaN μLEDs over soft organic LEDs because they are highly efficient and consume low power (22, 23), thereby producing high-brightness light emission with low thermal heating losses and inducing minimal heating effects on the cortical

tissue (24). In addition, the high intensity of light produced by GaN μLEDs is visible to the human eye even under the bright surgical lightning (25). To fabricate flexible GaN μLED arrays for both high resolution and broad spatial coverage, we developed a scalable process on 15.24-cm GaN/polycrystalline AlN–engineered Qromis Substrate Technology (QST) substrate (26, 27) and released ultrathin μLED arrays, some with 1024 pixels and some with 2048 pixels, embedded in polyimide layers (see fig. S1). GaN μLEDs with indium gallium nitride (InGaN) quantum wells emitted blue light with a peak wavelength of 450 nm (fig. S2). To simultaneously display and coregister normal and diseased cortical activity, we used ink-jet printing to deposit quantum dot color conversion (QDCC) inks made of indium phosphide (InP) quantum dots on the surface of the GaN μLEDs (fig. S2) (28). This allowed us to ensure that the GaN μLEDs emit multiple colors, enabling richer and more nuanced visual representations of neural activity patterns. The flexible GaN μLED arrays were then laminated on the back of the PtNRGrids grids (Fig. 1A) (20) to form the iEEG-microdisplay. The PtNRGrids were constructed on thin and brain-conformal parylene C substrates with thousands of channels that reliably recorded the spatiotemporal dynamics of brain activity at high resolution and with broad coverage (20, 29). Because both the flexible μLED array and μECoG were based on scalable and reconfigurable manufacturing processes, we matched their pitch and coverage for a single iEEG-microdisplay. Here, we discuss results based on displays with 32 mm–by–32 mm coverage and 1-mm pitch used for pig brains (Fig. 1A) and 5 mm–by–5 mm coverage with 0.15-mm pitch for rat brains (Fig. 1B). The single-color iEEG-microdisplay was composed of 1024 PtNR recording contacts and 1024 GaN μLED pixels. The dual-color iEEG-microdisplay comprised 2048 QDCC-printed GaN μLEDs with 0.4-mm vertical and 0.5-mm horizontal pitches and a corresponding PtNRGrid with 1024
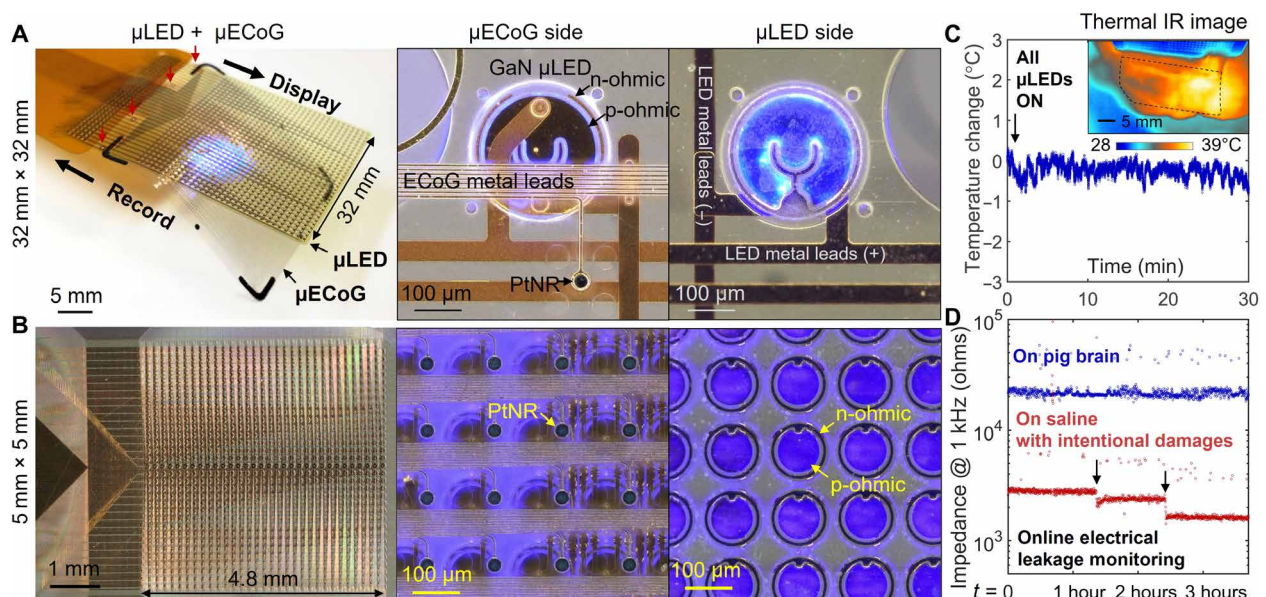
Fig. 1. Fabrication process and safety evaluation of the iEEG-microdisplay. (**A** and **B**) Overview images of the device structure and magnified optical microscopy images of 32 mm–by–32 mm (A) and 5 mm–by–5 mm (B) μLED + μECoG devices that integrated flexible μLED arrays with 1024 pixels and PtNRGrids with 1024 channels. (**C**) Thermal safety evaluation of the iEEG-microdisplay by monitoring the cortical surface temperature of the pig brain (n = 1) under 30 min of continuous operation of all the LEDs. (**D**) Electrical safety evaluation of iEEG-microdisplay by monitoring the impedance of the device with respect to the brain tissues over 3.7 hours on the pig's brain (n = 1).

contacts with 0.8-mm vertical and 0.5-mm horizontal pitches, both providing 12.8 mm–by–32 mm brain coverage (fig. S2, C and D). The µECoG grids used 30-µm diameter PtNR contacts with an average impedance of 30 kilohms at 1 kHz. The size of an individual GaN µLED varied depending on their intended use. Specifically, GaN µLEDs with a diameter of 220 µm were optimized for 1-mm pitch iEEG-microdisplay (Fig. 1A), whereas those with a diameter of 100 µm were designed for iEEG-microdisplays with higher densities, such as that used for the rat (Fig. 1B) or dual-color 2048 µLEDs used for the pig (fig. S2, C and D).

Part of the electrical input supplied to LEDs is not converted to light but lost as thermal energy. The consequential increase of the cortical surface temperature must be kept below 1°C (30, 31). To ensure that this is the case for our iEEG-microdisplay, we have characterized the thermal and electrical safety of the iEEG-microdisplay. In one experiment, we turned on all 2048 µLEDs at their maximum brightness possible with our LED driver chip as the iEEG-microdisplay was placed on top of the pig's brain for 30 min. The temperature was then monitored with an infrared (IR) imaging camera. No temperature changes within the measurement resolution of the IR camera (0.1°C) were observed (Fig. 1C). In addition, postmortem histochemical analysis of the same pig's brain showed undetectable differences in the structure of the cortical surface under the iEEG-microdisplay and the contralateral region (fig. S3): The top cortical layer was of comparable thickness, the neuronal density was similar, and the neuron shape was normal. However, when the same experiment was conducted on a rat's brain with the high-density iEEG-microdisplay whose pixel pitch was 0.15 mm, we observed a temperature increase of up to 6°C in less than 5 min when all 1024 µLEDs were turned on at maximum brightness. We therefore conducted a series of experiments to determine whether this temperature change could be minimized by adjusting the duty cycle of the µLEDs. We achieved acceptable brightness through these adjustments with less than 1°C increase in temperature (fig. S4).

Next, to continuously evaluate the integrity of the insulation materials for the µLEDs and impose preventive measures to shut down the iEEG-microdisplay upon insulation material degradation or failure, the impedance of all the electrically conducting elements (metal traces, ohmic contacts, and the GaN) of the µLEDs in relation to the brain tissue was monitored every 10 s throughout the entire 3.7-hour duration of pig brain recording. This test revealed no detectable changes in the impedance, indicating that no electrical leakage paths developed, and the conformal attachment was preserved for the duration of the experiment (Fig. 1D and fig. S5). To test the validity of our impedance monitoring setup and to ensure that it properly represents electrical leakage paths, scratches were purposely made on the surface of the µLED array. In this setting, a drop in impedance was observed whenever there was mechanical or electrical damage to the device (Fig. 1D), indicating that our impedance monitoring setup was reliable in detecting the presence of electrical leakage paths in the iEEG-microdisplay. The extended soak test of the iEEG-microdisplay in saline solution over 7 days revealed that the device's impedance remained stable throughout a week (fig. S6), further emphasizing the device's durability in a moist environment.

The iEEG-microdisplay allows anatomical mapping of functional M1/S1 boundaries on the surface of the brain

The precise localization of the central sulcus, the anatomical boundary between primary motor (M1) and somatosensory (S1) cortices,

is crucial in tumor and epileptogenic tissue resections in these brain regions. This boundary is identified at the point where SSEPs in response to peripheral nerve stimulation exhibit opposite polarity in their potentials commonly recognized by either a negative phase (P20) or a positive phase (N20) (32, 33). Commonly, the presence of pathological tissue can shift this functional boundary (FB) from its anatomical organization (7, 34). To test whether the iEEG-microdisplay can directly project the M1/S1 boundary from the surface of the brain on the basis of physiological signatures, we applied the 32 mm–by–32 mm iEEG-microdisplay across the midline of the pigs' brain covering both the left and right primary M1 and primary S1. To evoke SSEPs, we stimulated the peripheral nerves with subdermal twisted pair needles placed in the pig's left and right forelimbs (Fig. 2A; 10 mA, 1-ms biphasic pules). Small and short-duration stimulus artifacts were observed, followed by SSEPs within 10 to 50 ms after stimulation that exhibited phase reversal indicated by the red arrowheads in Fig. 2B (35). The iEEG-microdisplay revealed a cortical FB between the primary M1 cortex and primary S1 cortex depicted with a line of illuminated µLEDs in the hemisphere contralateral to stimulation (Fig. 2, C to H, and fig. S7). The displayed FB was in accordance with the offline analysis of raw potential waveforms done with the P20-N20 potential mapping (Fig. 2, D and G, and fig. S8) and correlation coefficient mapping (Fig. 2, E and H). When using a dual-color iEEG-microdisplay, FBs were represented by a change of color from green to red (Fig. 2, I and J).

The iEEG-microdisplay allows the identification of functional cortical columns from the surface of the brain

To demonstrate the advanced mapping and display capabilities of the iEEG-microdisplay, we conducted a localized sensory mapping on an anesthetized pig by administering electrical or air-puff sensory stimuli to different areas of the pig's face and limbs, thereby evoking high gamma responses on the brain's surface (Fig. 3A). The HGA was mapped for each of n = 50 trials, and the trial-averaged HGA mapping was updated and displayed—every 1 s—on the brain's surface whenever a new stimulus was administered. Subdermal electrical stimulation (2 mA, 1 ms, biphasic, bipolar) of left and right forelimbs, cheeks, and tongue was administered to reveal uniquely distinguishable cortical regions and simultaneously observe the anatomical features of the brain tissue underlying the iEEG-microdisplay (Fig. 3, B to G, and fig. S9). We hypothesized that local air-puff stimulation on the surface of the skin delivered through a microcapillary tube can lead to focal responses when compared with gross-sum activation of nerve fibers by electrical stimulation in the vicinity of the stimulating needle probes (36). With nerve electrical stimulation, HGA responses were less localized (Fig. 3D) compared with responses to air-puff stimulation of the tongue tip (Fig. 3G). These results were corroborated by responses of electrical or air-puff stimulations of the pig's snout depicted in waveforms (Fig. 3, H and I, and fig. S9) and the spatial mapping of the HGA (Fig. 3, J to L). The potential evoked by air-puff stimulation of two different snout positions (Fig. 3I) showed a single peak near 35 ms, whereas the electrically stimulated snout showed multiple peaks from 10 to 90 ms, the latter presumably because of the volumetric stimulation of multiple different types of sensory and motor neurons with varying latencies (37). The iEEG-microdisplay depicted relatively broader spatial maps of HGA responses evoked by electrical stimulation of the snout (Fig. 3J) and tightly localized HGA by air-puff stimulation of two different spots (Fig. 3, K and L) within the electrically responsive region of Fig. 3J. These

Tchoe et al., Sci. Transl. Med. 16, eadj7257 (2024)   24 April 2024

3 of 11
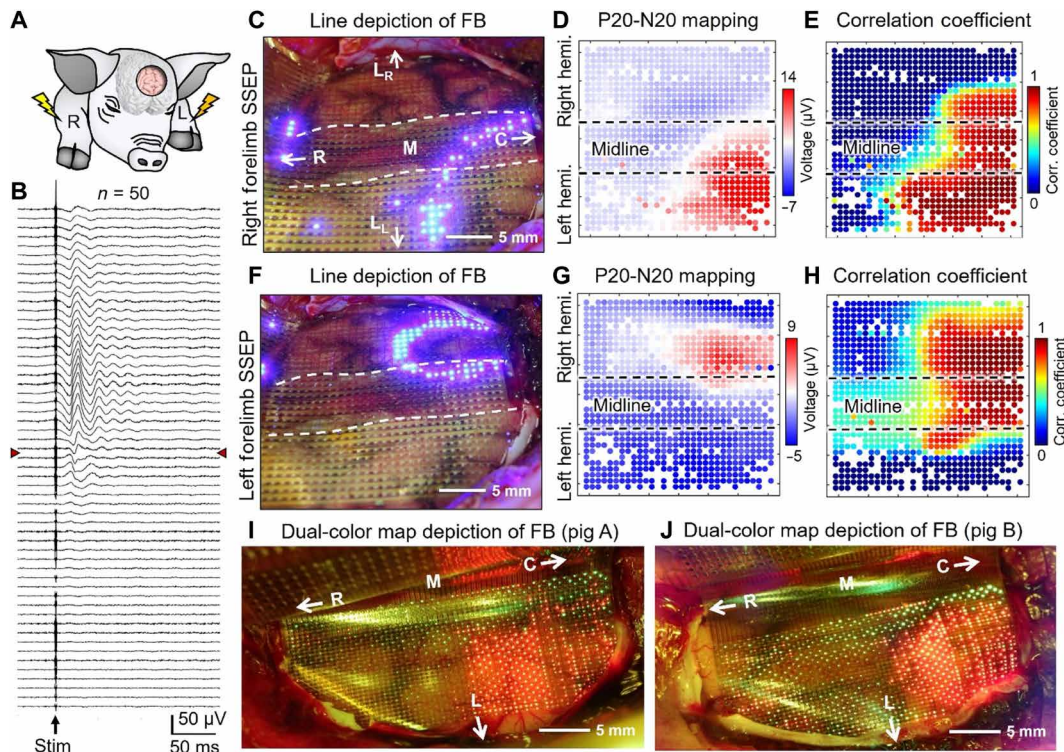
Fig. 2. Real-time mapping and display of the M1 and S1 border on the cortical surface of pig brains. (**A**) Schematics of the experiment depicting the electrical stimulation of the pig's left and right forelimbs (biphasic, bipolar pulse: 10 mA, 1 ms) while simultaneously recording SSEPs and displaying the M1/S1 boundary on the surface of the brain. (**B**) SSEP waveforms measured with dual-color iEEG-microdisplay across an individual row of μECoG contacts across the M1/S1 boundary. The red arrowheads indicate the phase reversal boundary. (**C**) Representative images of an active single-color (blue) 1024-channel iEEG-microdisplay for the detection M1/S1 function boundary using right-forelimb stimulation. The corresponding offline analysis results showing (**D**) P20-N20 potential and (**E**) correlation coefficient mapping. (**F**) Representative images of active single-color (blue) 1024-channel iEEG-microdisplay for the detection M1/S1 function using left-forelimb stimulation and (**G**) corresponding offline analysis of P20-N20 potential and (**H**) correlation coefficient mapping. (**I** and **J**) Representative images of dual-color iEEG-microdisplay of motor/sensory boundary observed from pig A (image taken under 550-nm blue light blocking lens) and pig B. (C to H) Results are presented from one of two pigs with bilaterally placed single-color μLEDs (pig #4). Figure S7 shows similar representative results from the second pig (pig #3). (I and J) Results are presented from two of two pigs with unilaterally placed dual-color μLEDs.

HGA mappings displayed on the brain surface were in agreement with the offline analysis on measured raw potential waveforms from PtNRGrids μECoG (Fig. 3, M and N) that shows spatial mapping of HGA together with trial-averaged raw waveforms ($n = 50$ trials).

Next, we applied the 5 mm–by–5 mm high-resolution iEEG-microdisplay to the barrel cortices of rats to isolate the location and boundaries of submillimeter-scale cortical columns (Fig. 3O). The rat barrel cortex is a well-studied system where specific sensory cortical columns have a one-to-one mapping with individual whiskers (38). While air-puffs stimulated the individual whiskers, we recorded and displayed the spatial map of trial-averaged ($n = 55$ trials) HGA. We observed that a small group of μLEDs were selectively lit up in distinct positions at submillimeter scale, indicating individual positions of cortical columns that correspond to each whisker (Fig. 3P). When all whiskers in the field-of-blow were air-puff stimulated, a larger group of μLEDs were lit up with a diameter near 3 mm, indicative of the extent of multiple whisker barrel cortices (Fig. 3P). When compared with the spatial mapping by offline analysis of recorded waveforms (Fig. 3Q), the spatial mapping of raw waveforms and HGA ($n = 55$ trials) (Fig. 3, R and S) were in agreement with the HGA displayed with iEEG-microdisplay.

The iEEG-microdisplay allows brain surface mapping of neuronal activity in response to DES

DES of the brain and observation of behavioral responses and afterdischarges inform the location and boundaries of diseased tissue and is typically carried out with a handheld bipolar cortical stimulator (Ojemann probe) (39). This procedure is generally performed on the exposed brain without any grid on the surface. Our iEEG-microdisplay was designed with large-diameter through-hole arrays (0.5-mm diameter with 1-mm pitch) throughout the grid (fig. S10). These perforations permitted the delivery of stimulation with the Ojemann probe to any position of the pig brain together with the simultaneous display of the extent of the resultant electrical potential and the brain's response (Fig. 4, A to C). We administered charge-balanced biphasic pulses of 3 mA and 50 Hz with varying durations between 0.1 and 1.9 s and recorded and displayed the root mean square (RMS) of the voltage brain wave responses within the frequency range of 10 to 59 Hz. The refresh rate of the iEEG-microdisplay was 40 Hz as we processed 25-ms data packets from 1024 channels and displayed the RMS map every 25 ms. Figure 4A shows the iEEG-microdisplay and the Ojemann proble placed on the pig's brain before stimulation. During brain stimulation, a large electrical potential was created, causing many μLEDs in the array to light up around
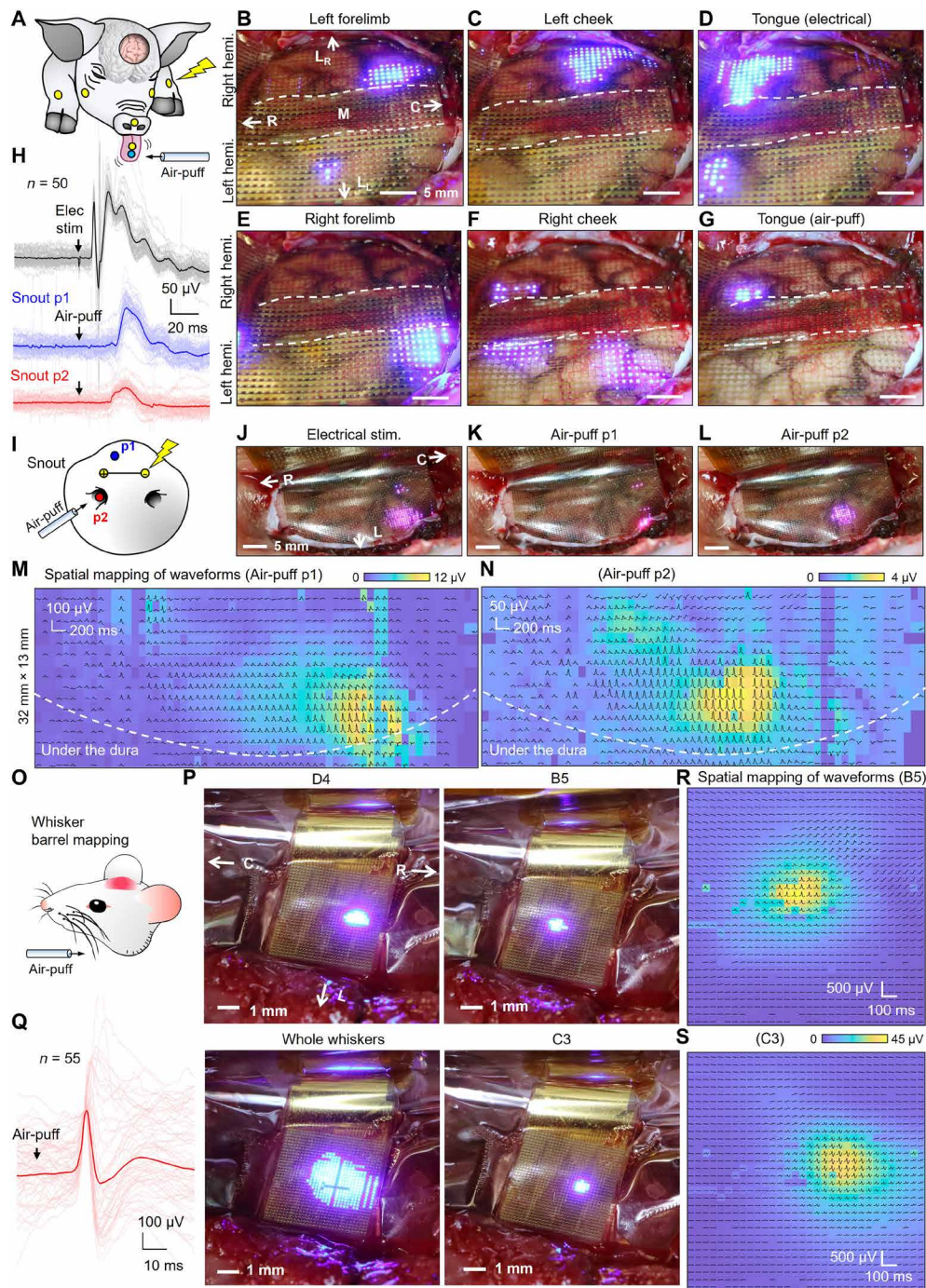
Fig. 3. Sensory mapping and display on the cortical surface of pig and rat brains. (**A**) Schematics showing the locations and type of sensory stimuli on different body parts of the pig. (**B** to **G**) HGA mapping of the electrical stimulation–evoked responses (*n* = 50 trials) of the left forelimb (B), left cheek (C), tongue (D), right forelimb (E), and right cheek (F). (G) HGA mapping evoked by air-puff stimulation of tongue tip from the same pig. (**H**) Trial average SSEP waveforms (*n* = 50 trials) overlaid with waveforms of individual trials under the electrical and air-puff stimulation of snout. (**I**) Schematics of electrical and air-puff stimulations of pig snout. HGA mapping evoked by (**J**) to (**L**). HGA mapping of electrical stimulation on the snout (J) and air-puff stimulation on the snout at positions p1 (K) and p2 (L). (**M** and **N**) Corresponding spatial mapping of HGA and trial-averaged raw waveforms (*n* = 50 trials) evoked by air-puff of snout at p1 (M) and p2 (N) positions. (**O**) Schematics of air-puff stimulation of rat whiskers. (**P**) HGA mapping of individual cortical column position of B5, C3, and D4 barrel cortices (*n* = 55 trials). Overall area of barrel cortices was displayed by the multiple whisker stimulation. (**Q**) Trial average SSEP waveforms (*n* = 55 trials) overlaid with waveforms of individual trials under the air-puff stimulation of whisker. (**R** and **S**) Spatial mapping of HGA and trial-averaged waveforms (*n* = 55 trials) by the air-puff stimulation of B5 (R) and C3 (S) whiskers. (B to H) Results are presented from one of two pigs with bilaterally placed single-color μLEDs (pig #4); fig. S9A shows representative results from the other pig (pig #3). (J to N) Representative results are presented from one of two pigs with a unilaterally placed dual-color μLEDs (pig #6); fig. S9B shows representative results from the second pig (pig #5). (P to S) Results are presented from one of three rats (rat #4). Figure S9 (C and D) shows representative results from rats #3 and #5, respectively.

each side of the bipolar probe (Fig. 4B). After the stimulation, we observed a poststimulus pattern around the bipolar probe near 200 ms (Fig. 4C). The RMS potential map observed in real time on the brain surface was in good agreement with the offline analysis of measured raw potential waveforms from PtNRGrids µECoG where the spatial map of raw waveforms was overlaid with the RMS potential map (Fig. 4, D and E).

In addition to the stimulation of the brain surface with an Ojemann probe, depth electrode stimulation was also used to map corticocortical

structures. To this end, we inserted a stereoelectroencephalography (sEEG) probe (0.8-mm diameter, contact spacing of 6 mm) into the depth of the brain (Fig. 4F) next to the iEEG-microdisplay (see the position marked in Fig. 4, F and G). We then applied bipolar, biphasic stimulation pulses (4 mA, 0.5 ms, single pulse) between adjacent contacts at depths of 9 and 3 mm, respectively. Under a single pulse stimulation, a population of pink LEDs lit up around the sEEG stimulation site, indicating a spatial display of poststimulus potentials on the brain surface (Fig. 4G). Here, a dual-color iEEG-microdisplay

Fig. 4. Display of electrical potentials in response to DES on the cortical surface of pig brains. (**A** to **C**) Shown are representative images of the display of electrical activity before (B), during the electrical stimulation (3 mA, 50 Hz) (A), and after stimulation (200 ms) (C). (**D** and **E**) Offline analysis of measured raw potential waveforms from PtNRGrids µECoG and RMS potential map (10 to 59 Hz) during the stimulation (−200 to 0 ms) (D) and after the stimulation (−10 to 200 ms) (E); the RMS potential map for (E) was obtained between 20 and 40 ms after stimulus. (**F** and **G**) Shown are potential maps displayed on the cortical surface with "blue" color (F) illustrating the HGA corresponding to forelimb and "pink" color (G) illustrating the online potential map evoked by the 4-mA electrical stimulations by sEEG electrode between the pair of electrodes at the depth of 9 and 3 mm. (**H**) Waveform mapping (−100 to 300 ms) together with RMS potential map (35 to 60 ms, 10 to 59 Hz) after a 4-mA single pulse. (A to E) Representative results are presented from one of two pigs with bilaterally placed and single-color µLEDs (pig #3, see also movie S1). Movie S5 shows electrical stimulation through iEEG-microdisplay in the second pig (pig #4). (F to H) Results are presented from one of two pigs with unilaterally placed dual-color µLEDs (pig #5, see also movie S2). Movie S6 shows similar stimulation results from the second pig (pig #6).
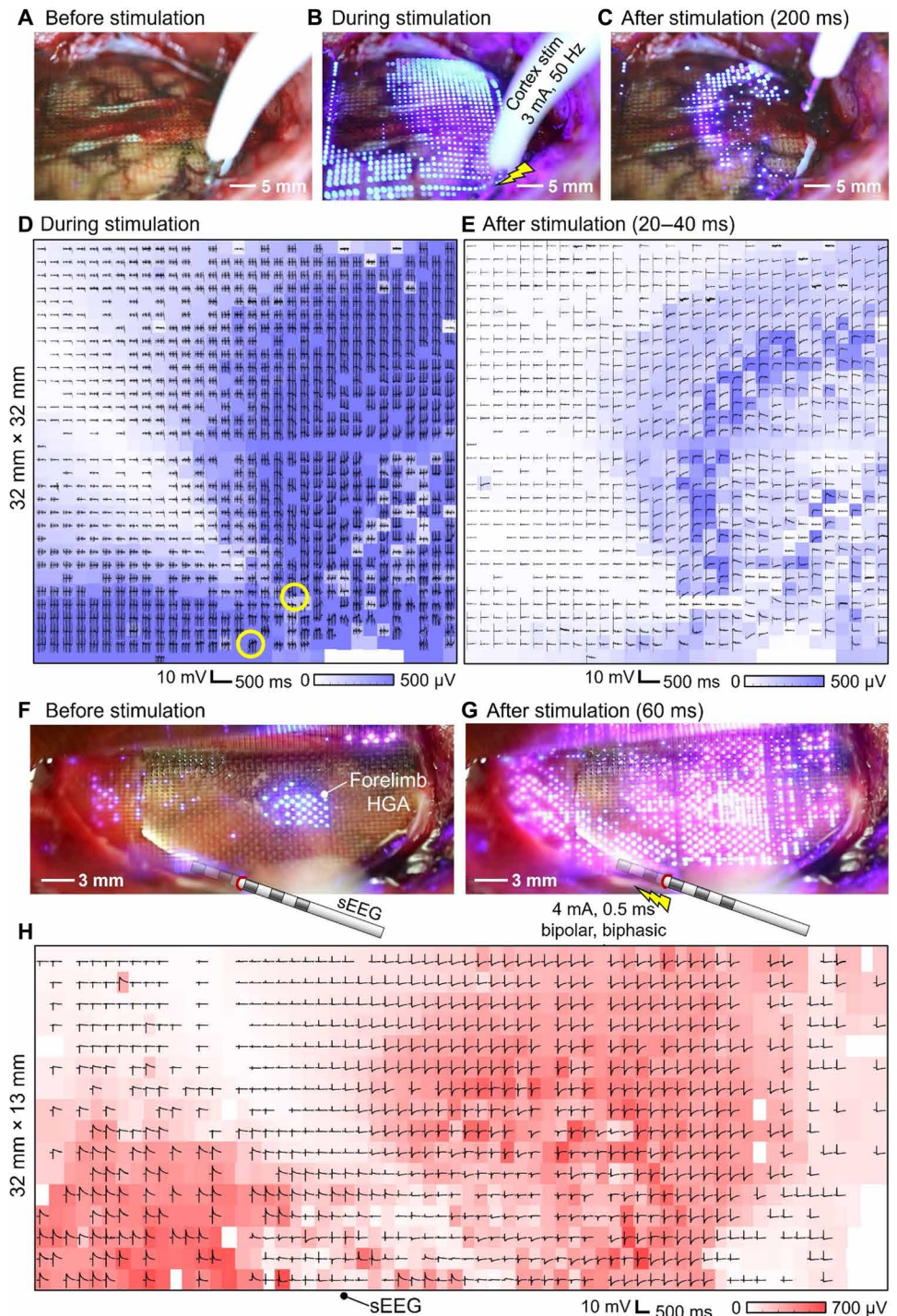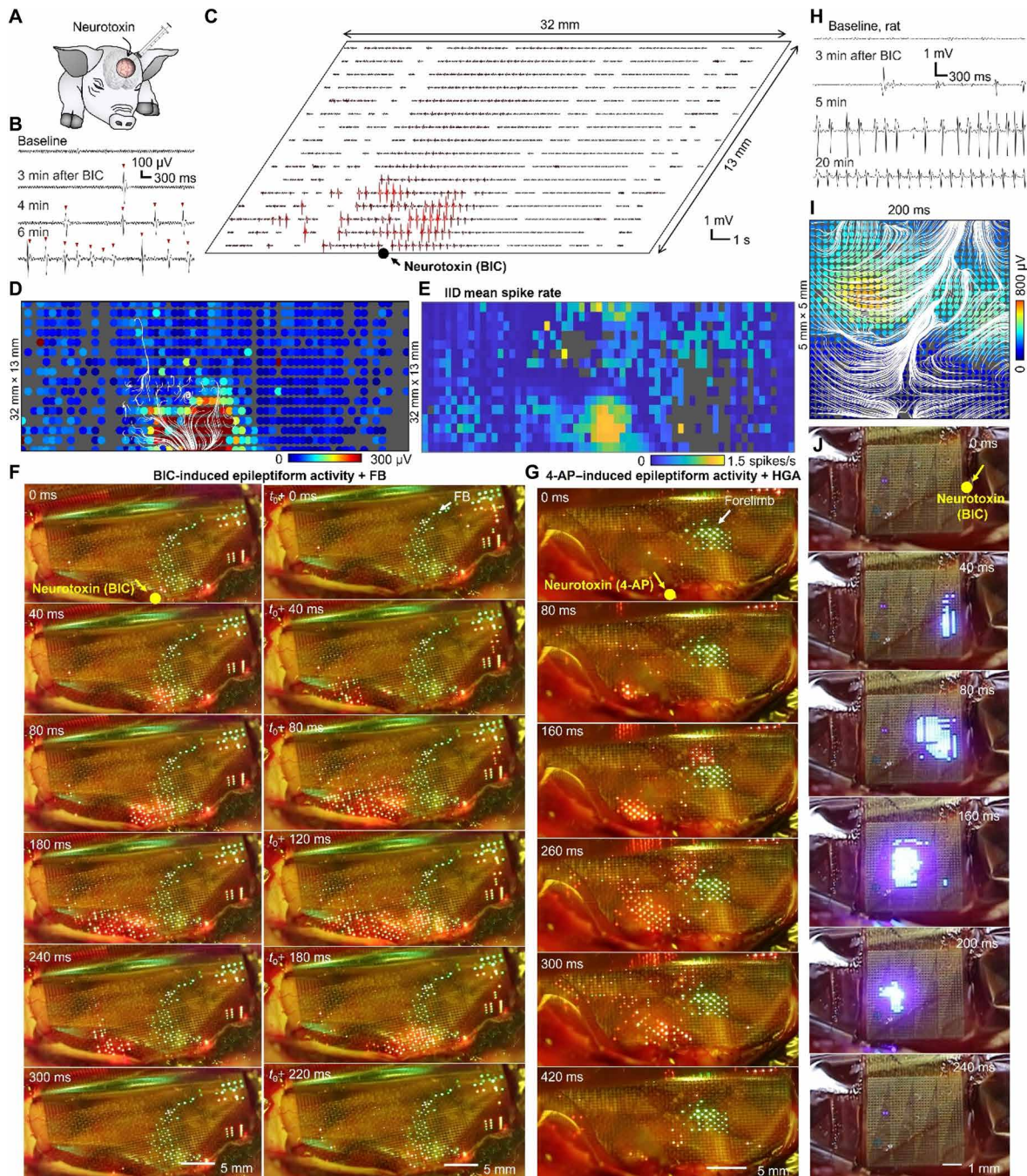
Fig. 5. Mapping of epileptiform activity on the cortical surface of pig and rat brains. (**A**) Schematics of experimental setup for evoking epileptiform activities on the pig brain by BIC and 4-AP. (**B**) ECoG waveforms of baseline activity before and 3, 4, and 6 min after the application of BIC. (**C**) Spatial mapping of waveforms showing locally induced epileptiform activities around the topical application point of BIC crystals. (**D**) Spatial potential mapping of epileptiform spike overlaid with white streamlines depicting the propagating direction of the brain wave at 0 ms. (**E**) Spatial mapping of mean spike rate of the detected interictal discharges. (**F**) Series of potential maps displayed on the cortical surface (under 550-nm blue blocking lens) with static "green" color showing the motor/sensory functional boundary and dynamic "red" color showing the online potential map of putative epileptiform activity under the BIC application on the cortex. BIC application point is marked as a yellow dot in the first image. An outward propagating epileptiform wave from BIC application point was observed (left column), and after a short interval, t_0, an inward propagating epileptiform wave toward the BIC application point was observed (middle column). (**G**) 4-AP–induced putative epileptiform activities on a different pig with green spot indicating the cortical area responsive to forelimb stimulation as identified with HGA mapping. (**H**) Waveforms of baseline activity and epileptiform activity induced on the rat brain by BIC over 3, 5, and 20 min. (**I**) Spatial mapping of putative IIDs together with the white streamlines showing the propagating direction of the putative epileptiform activities. (**J**) Displaying the putative epileptiform activities induced by BIC application. The original BIC application point is marked as a yellow dot. (A to E) Representative results are presented from the pig with unilaterally placed dual-color µLEDs. (F to H) Results are presented from one of two rats (rat #6). Movie S7 shows results from the second rat (rat #4).

with 2048 µLEDs displayed a statically lit HGA corresponding to the forelimb in blue and the real-time evolution of the RMS potentials in pink (Fig. 4F). The spatial pattern of the responses observed on the iEEG-microdisplay was in good agreement with the offline analysis, which overlaid the poststimulus RMS potential map (35 to 60 ms, 10 to 59 Hz) together with the spatial map of waveforms including the stimulation pulse (−100 to 300 ms) (Fig. 4H). These results illustrate that the iEEG-microdisplay provided real-time feedback of stimulation responses directly from the surface of the brain (movies S1 and S2).

The iEEG-microdisplay allows the monitoring of pathological wave dynamics

A final important feature of the iEEG-microdisplay is its ability to facilitate high-resolution mapping of pathological brain activity. For example, the precise intraoperative neuromonitoring to detect the onset zones of seizures and patterns of their spread is essential for successful treatment (40). To demonstrate that pathological brain activity, such as epileptiform activity, could be displayed using the iEEG-microdisplay, we placed the display over the anesthetized pig's brain and artificially induced epileptic seizures by applying neurotoxins on the brain underlying the display (Fig. 5A). This procedure included the administration of three types of neurotoxins, with each toxin administered to separate animals: (i) bicuculline (BIC) crystals that were topically applied on the brain surface and (ii) the subcortical injection of 4-aminopyrodine (4-AP) or penicillin-G (Pen-G). All three types of neurotoxins induced epileptiform activities, whereas BIC induced the most prominent responses, showing large-amplitude epileptiform activities (approximately 0.5 mV peak to peak) (Fig. 5B). After the initial observation of the epileptiform activity (which occurred 3 min after the application of BIC), the frequency of epileptiform activities rapidly increased over each subsequent minute (Fig. 5C). Six minutes after the BIC application, spatial mapping of large voltage deflections (10 to 59 Hz) through RMS detections revealed distinct and repetitive voltage deflections (likely correlated with epileptiform activity) within a few millimeters around the BIC application point during the case.

We conducted further investigation into the origin and spatiotemporal dynamics of epileptiform activity using streamlines to indicate the propagating direction of brain waves (20). The spatial mapping of epileptiform discharge events was analyzed using the spatial mapping of potentials in band-pass–filtered data (10 to 59 Hz) and streamlines derived from phase gradient analysis (41). The epileptiform activity (Fig. 5D) revealed an epileptiform discharge wave originating near the BIC application site, which then propagated outward as represented by the white streamlines (Fig. 5D). Conversely, the second epileptiform event occurred about 500 ms after the first and showed the epileptiform discharge wave propagating in the reverse direction, back toward the origin of the first epileptiform discharge. To ascertain whether the observed epileptiform waves were pathological interictal discharges (IIDs), we used offline automatic detection algorithms commonly used for identifying IIDs (42) combined with visual confirmation by an experienced epileptologist (S.S.C.). We found overlap between the detected IIDs and the spatially located RMS detections near the site of the BIC application (Fig. 5, C to E). This spatial mapping of the spike rate for the detected voltage deflections possibly correlating with IIDs (Fig. 5E) correlated with the displayed RMS-measured voltage changes on the surface of the pig's brain using the iEEG-microdisplay (Fig. 5F). The images were captured

under blue-light blocking glass (>550-nm long-pass filter; fig. S2) to enhance the distinction between the green and red colors displayed by the dual-color µLED arrays. While displaying the M1/S1 boundary as a static green line, the large voltage deflections possibly correlating with IIDs were shown in real time in red. Using this iEEG-microdisplay, a pathological wave likely correlating with an IID was observed originating near the BIC application site, which propagated to the left side. A consecutive event then showed these voltage deflections propagating back in the reverse direction (Fig. 5F and movie S3). These observations are consistent with the findings from our offline analysis (Fig. 5, D and E). The voltage waves likely correlating with IIDs propagated back and forth repeatedly from the BIC application site throughout the entire 1-hour experiment duration. Moreover, when another BIC dose was administered on the rightmost side of the grid, a large voltage wave originating and propagating from the new application site was observed (fig. S11). Similar propagating behavior of pathological waves was observed when 4-AP (Fig. 5G) or Pen-G (fig. S12) was injected subcortically.

For future clinical application of the iEEG-microdisplay, it would be essential to detect and display pathological activities that would be coregistered to functional regions in the cortex. To this end, the cortical regions responding to electrical stimulation of the forelimb were mapped and displayed as a static green spot, whereas real-time evolution of the pathological activity was shown dynamically as it occurred in red (Fig. 5G). The large repetitive voltage waveforms that are likely IIDs originated near the 4-AP injection site and propagated and spread away from that site. This shows that the iEEG-microdisplay technology could be used to communicate multiple types of information, display functional boundaries in green color, and show high-resolution real-time videos of pathological waves with red.

Last, we evaluated the iEEG-microdisplay's capacity to detect and display fine-scale pathological activity at a high resolution. The iEEG-microdisplay was positioned on the barrel cortex of a rat after which epileptiform activity was induced by topical application of BIC next to the cortical surface next to the iEEG-microdisplay. Similar to the case of the pig, the first voltage event, which is a putative IID, occurred 3 min after administering BIC to the barrel cortex of the rat. The frequency of these voltage deflections increased to four spikes per minute at the 5-min mark (Fig. 5H), with a substantial peak-to-peak amplitude of 3 mV. After 20 min had elapsed since the first BIC dose, the voltage deflections amplitude decreased to 1 mV peak to peak, and the same spiking rate of four spikes per minute continued from the 5-min mark. We also applied propagating wave analysis to the observed events by overlaying the potential map (filtered in the frequency range of 10 to 59 Hz) and streamlines representing the instantaneous propagating characteristics of pathological brain waves analyzed by the phase gradient (Fig. 5I). These putative IIDs on the rat brain surface were visible in real time, as shown by the series of images at each time point (Fig. 5J and movie S4). We repeatedly observed the IIDs originating near the BIC application site and propagating and spreading out to the left side. These findings demonstrate that the iEEG-microdisplay allows the display of submillimeter-scale pathological wave dynamics in real time.

DISCUSSION

We developed an iEEG-microdisplay that allows the display of the dynamics of brain cortical activity in real time. The iEEG-microdisplay is composed of flexible 1024 or 2048 µLED arrays combined with

1024-channel PtNRGrids and associated hardware and software for real-time display. This design enabled mapping of normal and pathological activities in submillimeter resolution over the extent of centimeter range. With its high spatial and temporal resolution of neural activity and real-time visual feedback, the iEEG-microdisplay offers a potential improvement over current intraoperative brain mapping practices. The flexible μLED arrays built on thin, semitransparent, and conformal polyimide substrates can be reconfigured in pitch to achieve wide cortical coverage. Multiple colors can be displayed to indicate different types of cortical activity. The iEEG-microdisplay is scalable and provides real-time feedback on neural activities in response to external stimulation. In the future, the iEEG-microdisplay can be used to visualize healthy and diseased brain regions and their boundaries directly from the surgical field (fig. S14).

However, our study has limitations. The close proximity of the μLED system and μECoG grid led to interference, causing high-frequency noise to be added to the ECoG signals when the μLED system was powered on. This interference resulted from the microdisplay being driven by high-frequency 5-V pulses, even when the LEDs were not emitting light. The noise appeared as multiple peaks in the power spectral density plots, typically starting at 98.63 Hz and its harmonics (see fig. S13). Despite these noise issues, we were still able to effectively extract meaningful neurophysiological signals, displaying important cortical functional boundaries and propagation of IIDs. To further reduce the noise, we plan to implement customized hardware to drive the μLEDs at higher pulse rates in future iterations of the device. This adjustment would result in the noise peaks currently at 98.63 and 197.37 Hz being shifted to frequencies above 200 Hz. By ensuring that all noise peaks surpass the high gamma frequency bands, we can implement a low-pass filter with a cutoff below 200 Hz to effectively isolate brain wave signals with minimal noise. In addition, we envision implementing in future iterations ground traces between LED line traces that can be used to further attenuate the resulting electromagnetic noise induced by the traces used to switch the LEDs.

To translate this technology to human application, the system must be able to perform continuous and high-sensitivity measurements for the detection of leakage currents preferably on each metal line. This approach could replace the intermittent impedance measurements performed every 10 s. Although the PtNRGrid passed the biocompatibility, sterility, and packaging requirements for clinical translation, these tests must be performed on the completely assembled iEEG-microdisplay for use in humans. For full-color display, lamination of three red, green, and blue GaN μLEDs will be required as opposed to the color conversion scheme presented here for binary display of normal and pathological brain activity. With the increase of the spatial resolution toward high-definition display, the transparency of the iEEG-microdisplay can be compromised. However, with the high-frame display, it is possible to project the anatomical features as a static image on the iEEG-microdisplay and simultaneously display normal and pathological activity in real time.

The future dissemination of the iEEG-microdisplay should also account for its cost. We estimate the cost of goods for a single PtNRGrid to be approximately $500—using the 17.78 cm–by–17.78 cm glass plate substrate—and for a single GaN μLED array to be approximately $600 on the 15.24-cm GaN-on-QST substrate and using equipment in our research facilities. Accounting for labor cost, the current overall cost of the iEEG-microdisplay will be higher than the cost of clinical ECoG grid technology yet reasonable. The whole GaN μLED array transfer developed here is low cost when compared with flip-chip array integration of individual μLEDs. The concept of the iEEG-microdisplay encompasses the combination of ECoG technology and of LED technology irrespective of the materials used provided that they offer comparable or better performance than what is presented here. At the large dissemination scale, we envision the cost of iEEG-microdisplay to be comparable to or lower than that of a cell phone screen, which is currently a few tens of dollars. An overall end-to-end solution with software display and analysis will likely have a cost that is comparable to that of a cell phone. Last, it would be desirable to excise tissue while the iEEG-microdisplay is placed on the brain's surface without interfering with its function. We envision that creating a foldable portion within the iEEG-microdisplay can create a window-in-grid for operation. In addition, most tissue excisions in the brain are performed with ultrasonic vibration and suction and, as such, the potential integration of ultrasound microtransducers next to the PtNRGrid may provide the capability of performing micro-excisions for diseased tissue without severely compromising its conformity. With light directed toward the cortical surface, the iEEG-microdisplay could be used for high-resolution optogenetic stimulation. In conclusion, the iEEG-microdisplay has the potential to improve brain activity mapping for basic neuroscience as well as neurosurgical practices.

MATERIALS AND METHODS
Study design
The objectives of the study were to design, fabricate, and validate the effectiveness and utility of the iEEG-microdisplay for real-time visualization of cortical activity. The methodology involved fabricating the iEEG-microdisplay, which included the fabrication of flexible μLED arrays and of μECoG electrode grids and their integration, and testing of its effectiveness for real-time brain activity mapping in both pigs and rats. Key metrics evaluated included device stability, precision in activity mapping, and safety of operation validated by postmortem histology. The ultimate goal was to validate the iEEG-microdisplay as an effective instrument for offering high-resolution, real-time visualization of brain activity that holds promise for improving neurosurgical outcomes in future studies. We used proof-of-concept experiments in rats and pigs to test the capacity of the iEEG-microdisplay to monitor brain activity and functional borders in the form of spatially registered light patterns on the brain surface. We successfully recorded surface μECoG signals and displayed activity with LEDs in real time from six rats and six pigs. Given the exploratory and qualitative focus of our study on the iEEG-microdisplay, sample size was not predetermined. The data collected from animals using early prototypes of the iEEG-microdisplay were excluded from the study. The number of trials in a specific animal model recording was determined when functional cortical mapping reached its saturation point. Each experimental paradigm included controls for acquiring a baseline recording before or throughout the given recording period. Data acquisition was not blinded, and we did not include a randomization of subject selection in this study. No statistical tests were used in this study because our aim was to qualitatively assess the iEEG-microdisplay's functionality and its application in real-time cortical activity visualization. All procedures for the rat and pig experiment were approved by the University of California, San Diego Institutional Animal Care and Use Committee under protocol S16020 and S19030, respectively.

Supplementary Materials

This PDF file includes:

Materials and Methods
Figs. S1 to 14
Tables S1 and S2
References (*43–45*)

Other Supplementary Material for this manuscript includes the following:

Data file S1
Movies S1 to S7
MDAR Reproducibility Checklist

REFERENCES AND NOTES

1. P. Karschnia, M. A. Vogelbaum, M. van den Bent, D. P. Cahill, L. Bello, Y. Narita, M. S. Berger, M. Weller, J.-C. Tonn, Evidence-based recommendations on categories for extent of resection in diffuse glioma. *Eur. J. Cancer* **149**, 23–33 (2021).
2. D. P. Cahill, Extent of resection of glioblastoma: A critical evaluation in the molecular era. *Neurosurg. Clin. N. Am.* **32**, 23–29 (2021).
3. S. Krishna, A. Choudhury, M. B. Keough, K. Seo, L. Ni, S. Kakaizada, A. Lee, A. Aabedi, G. Popova, B. Lipkin, C. Cao, C. N. Gonzales, R. Sudharshan, A. Egladyous, N. Almeida, Y. Zhang, A. M. Molinaro, H. S. Venkatesh, A. G. S. Daniel, K. Shamardani, J. Hyer, E. F. Chang, A. Findlay, J. J. Phillips, S. Nagarajan, D. R. Raleigh, D. Brang, M. Monje, S. L. Hervey-Jumper, Glioblastoma remodelling of human neural circuits decreases survival. *Nature* **617**, 599–607 (2023).
4. D. J. Englot, S. J. Han, M. S. Berger, N. M. Barbaro, E. F. Chang, Extent of surgical resection predicts seizure freedom in low-grade temporal lobe brain tumors. *Neurosurgery* **70**, 921–928 (2012).
5. M. Mohan, S. Keller, A. Nicolson, S. Biswas, D. Smith, J. Osman Farah, P. Eldridge, U. Wieshmann, The long-term outcomes of epilepsy surgery. *PLOS One* **13**, e0196274 (2018).
6. P. Shah, J. M. Bernabei, L. G. Kini, A. Ashourvan, J. Boccanfuso, R. Archer, K. Oechsel, S. R. Das, J. M. Stein, T. H. Lucas, D. S. Bassett, K. A. Davis, B. Litt, High interictal connectivity within the resection zone is associated with favorable post-surgical outcomes in focal epilepsy patients. *NeuroImage Clin.* **23**, 101908 (2019).
7. H. Duffau, J. P. Sichez, S. Lehéricy, Intraoperative unmasking of brain redundant motor sites during resection of a precentral angioma: Evidence using direct cortical stimulation. *Ann. Neurol.* **47**, 132–135 (2000).
8. H. Duffau, L. Capelle, J.-P. Sichez, T. Faillot, L. Abdennour, J.-D. Law Koune, S. Dadoun, A. Bitar, F. Arthuis, R. Van Effenterre, D. Fohanno, Intra-operative direct electrical stimulations of the central nervous system: The Salpêtrière experience with 60 patients. *Acta Neurochir.* **141**, 1157–1167 (1999).
9. S. S. Skirboll, G. A. Ojemann, M. S. Berger, E. Lettich, H. R. Winn, Functional cortex and subcortical white matter located within gliomas. *Neurosurgery* **38**, 678–685 (1996).
10. T. Yang, S. Hakimian, T. H. Schwartz, Intraoperative electrocorticography (ECog): Indications, techniques, and utility in epilepsy surgery. *Epileptic Disord.* **16**, 271–279 (2014).
11. H. Duffau, M. Lopes, F. Arthuis, A. Bitar, J. Sichez, R. Van Effenterre, L. Capelle, Contribution of intraoperative electrical stimulations in surgery of low grade gliomas: A comparative study between two series without (1985–96) and with (1996–2003) functional mapping in the same institution. *J. Neurol. Neurosurg. Psychiatry* **76**, 845–851 (2005).
12. S. Borchers, M. Himmelbach, N. Logothetis, H.-O. Karnath, Direct electrical stimulation of human cortex—The gold standard for mapping brain functions? *Nat. Rev. Neurosci.* **13**, 63–70 (2012).
13. J. R. Swift, W. G. Coon, C. Guger, P. Brunner, M. Bunch, T. Lynch, B. Frawley, A. L. Ritaccio, G. Schalk, Passive functional mapping of receptive language areas using electrocorticographic signals. *Clin. Neurophysiol.* **129**, 2517–2524 (2018).
14. A. A. Aabedi, B. Lipkin, J. Kaur, S. Kakaizada, C. Valdivia, S. Reihl, J. S. Young, A. T. Lee, S. Krishna, M. S. Berger, E. F. Chang, D. Brang, S. L. Hervey-Jumper, Functional alterations in cortical processing of speech in glioma-infiltrated cortex. *Proc. Natl. Acad. Sci. U.S.A.* **118**, e2108959118 (2021).
15. H. S. Venkatesh, W. Morishita, A. C. Geraghty, D. Silverbush, S. M. Gillespie, M. Arzt, L. T. Tam, C. Espenel, A. Ponnuswami, L. Ni, P. J. Woo, K. R. Taylor, A. Agarwal, A. Regev, D. Brang, H. Vogel, S. Hervey-Jumper, D. E. Bergles, M. L. Suvà, R. C. Malenka, M. Monje, Electrical and synaptic integration of glioma into neural circuits. *Nature* **573**, 539–545 (2019).
16. M. M. Haglund, M. S. Berger, M. Shamseldin, E. Lettich, G. A. Ojemann, Cortical localization of temporal lobe language sites in patients with gliomas. *Neurosurgery* **34**, 567–576 (1994).
17. D. G. Southwell, S. L. Hervey-Jumper, D. W. Perry, M. S. Berger, Intraoperative mapping during repeat awake craniotomy reveals the functional plasticity of adult cortex. *J. Neurosurg.* **124**, 1460–1469 (2016).
18. T. Kaiju, M. Inoue, M. Hirata, T. Suzuki, High-density mapping of primate digit representations with a 1152-channel µECoG array. *J. Neural Eng.* **18**, 036025 (2021).
19. C.-H. Chiang, C. Wang, K. Barth, S. Rahimpour, M. Trumpis, S. Duraivel, I. Rachinskiy, A. Dubey, K. E. Wingel, M. Wong, N. S. Witham, T. Odell, V. Woods, B. Bent, W. Doyle, D. Friedman, E. Bihler, C. F. Reiche, D. G. Southwell, M. M. Haglund, A. H. Friedman, S. P. Lad, S. Devore, O. Devinsky, F. Solzbacher, B. Pesaran, G. Cogan, J. Viventi, Flexible, high-resolution thin-film electrodes for human and animal neural research. *J. Neural Eng.* **18**, 045009 (2021).
20. Y. Tchoe, A. M. Bourhis, D. R. Cleary, B. Stedelin, J. Lee, K. J. Tonsfeldt, E. C. Brown, D. A. Siler, A. C. Paulk, J. C. Yang, H. Oh, Y. G. Ro, K. Lee, S. M. Russman, M. Ganji, I. Galton, S. Ben-Haim, A. M. Raslan, S. A. Dayeh, Human brain mapping with multithousand-channel PtNRGrids resolves spatiotemporal dynamics. *Sci. Transl. Med.* **14**, eabj1441 (2022).
21. S. P. DenBaars, D. Feezell, K. Kelchner, S. Pimputkar, C.-C. Pan, C.-C. Yen, S. Tanaka, Y. Zhao, N. Pfaff, R. Farrell, M. Iza, S. Keller, U. Mishra, J. S. Speck, S. Nakamura, Development of gallium-nitride-based light-emitting diodes (LEDs) and laser diodes for energy-efficient lighting and displays. *Acta Mater.* **61**, 945–951 (2013).
22. J. Shin, H. Kim, S. Sundaram, J. Jeong, B.-I. Park, C. S. Chang, J. Choi, T. Kim, M. Saravanapavanantham, K. Lu, S. Kim, J. M. Suh, K. S. Kim, M.-K. Song, Y. Liu, K. Qiao, J. H. Kim, Y. Kim, J.-H. Kang, J. Kim, D. Lee, J. Lee, J. S. Kim, H. E. Lee, H. Yeon, H. S. Kum, S.-H. Bae, V. Bulovic, K. J. Yu, K. Lee, K. Chung, Y. J. Hong, A. Ougazzaden, J. Kim, Vertical full-colour micro-LEDs via 2D materials-based layer transfer. *Nature* **614**, 81–87 (2023).
23. J. J. Wierer Jr., N. Tansu, III-nitride micro-LEDs for efficient emissive displays. *Laser Photonics Rev.* **13**, 1900141 (2019).
24. R. Rajalingham, M. Sorenson, R. Azadi, S. Bohn, J. J. DiCarlo, A. Afraz, Chronically implantable LED arrays for behavioral optogenetics in primates. *Nat. Methods* **18**, 1112–1116 (2021).
25. N. Zhu, S. Mondal, S. Gao, S. Achilefu, V. Gruev, R. Liang, Engineering light-emitting diode surgical light for near-infrared fluorescence image-guided surgical systems. *J. Biomed. Opt.* **19**, 076018 (2014).
26. A. Tanaka, W. Choi, R. Chen, R. Liu, W. M. Mook, K. L. Jungjohann, P. K. Yu, S. A. Dayeh, Structural and electrical characterization of thick GaN layers on Si, GaN, and engineered substrates. *J. Appl. Phys.* **125**, 082517 (2019).
27. V. Odnoblyudov, O. Aktas, C. Basceri, in *Electrochemical Society Meeting Abstracts prime2020* (The Electrochemical Society Inc., 2020), pp. 1814–1814.
28. Z. Hu, Y. Yin, M. U. Ali, W. Peng, S. Zhang, D. Li, T. Zou, Y. Li, S. Jiao, S.-J. Chen, C.-Y. Lee, H. Meng, H. Zhou, Inkjet printed uniform quantum dots as color conversion layers for full-color OLED displays. *Nanoscale* **12**, 2103–2110 (2020).
29. M. Ganji, A. C. Paulk, J. C. Yang, N. W. Vahidi, S. H. Lee, R. Liu, L. Hossain, E. M. Arneodo, M. Thunemann, A. Shigyo, A. Tanaka, S. B. Ryu, S. W. Lee, Y. Tchoe, M. Marsala, A. Devor, D. R. Cleary, J. R. Martin, H. Oh, V. Gilja, T. Q. Gentner, S. I. Fried, E. Halgren, S. S. Cash, S. A. Dayeh, Selective formation of porous Pt nanorods for highly electrochemically efficient neural electrode interfaces. *Nano Lett.* **19**, 6244–6254 (2019).
30. T. M. Seese, H. Harasaki, G. M. Saidel, C. R. Davies, Characterization of tissue morphology, angiogenesis, and temperature in the adaptive response of muscle tissue to chronic heating. *Lab. Invest.* **78**, 1553–1562 (1998).
31. S. Kim, P. Tathireddy, R. A. Normann, F. Solzbacher, Thermal impact of an active 3-D microelectrode array implanted in the brain. *IEEE Trans. Neural Syst. Rehabil. Eng.* **15**, 493–501 (2007).
32. J. Romstöck, R. Fahlbusch, O. Ganslandt, C. Nimsky, C. Strauss, Localisation of the sensorimotor cortex during surgery for brain tumours: Feasibility and waveform patterns of somatosensory evoked potentials. *J. Neurol. Neurosurg. Psychiatry* **72**, 221–229 (2002).
33. C. Cedzich, M. Taniguchi, S. Schäfer, J. Schramm, Somatosensory evoked potential phase reversal and direct motor cortex stimulation during surgery in and around the central region. *Neurosurgery* **38**, 962–970 (1996).
34. A. Haseeb, E. Asano, C. Juhász, A. Shah, S. Sood, H. T. Chugani, Young patients with focal seizures may have the primary motor area for the hand in the postcentral gyrus. *Epilepsy Res.* **76**, 131–139 (2007).
35. C. C. Wood, D. D. Spencer, T. Allison, G. McCarthy, P. D. Williamson, W. R. Goff, Localization of human sensorimotor cortex during surgery by cortical surface recording of somatosensory evoked potentials. *J. Neurosurg.* **68**, 99–111 (1988).
36. E. F. Civillico, D. Contreras, Comparison of responses to electrical stimulation and whisker deflection using two different voltage-sensitive dyes in mouse barrel cortex in vivo. *J. Membr. Biol.* **208**, 171–182 (2005).
37. S. Maier, U. Goebel, S. Krause, C. Benk, M. A. Schick, H. Buerkle, F. Beyersdorf, F. A. Kari, J. Wollborn, Somatosensory and transcranial motor evoked potential monitoring in a porcine model for experimental procedures. *PLOS One* **13**, e0205410 (2018).
38. A. Keller, in *The Barrel Cortex of Rodents* (Springer, 1995), pp. 221–262.
39. G. A. Ojemann, Brain organization for language from the perspective of electrical stimulation mapping. *Behav. Brain Sci.* **6**, 189–206 (1983).
40. E. L. So, Integration of EEG, MRI, and SPECT in localizing the seizure focus for epilepsy surgery. *Epilepsia* **41** (Suppl. 3), S48–S54 (2000).

Tchoe *et al.*, *Sci. Transl. Med.* **16**, eadj7257 (2024)   24 April 2024

10 of 11

41. D. Rubino, K. A. Robbins, N. G. Hatsopoulos, Propagating waves mediate information transfer in the motor cortex. *Nat. Neurosci.* **9**, 1549–1557 (2006).

42. R. Janca, P. Jezdik, R. Cmejla, M. Tomasek, G. A. Worrell, M. Stead, J. Wagenaar, J. G. R. Jefferys, P. Krsek, V. Komarek, P. Jiruska, P. Marusic, Detection of interictal epileptiform discharges using signal envelope distribution modelling: Application to epileptic and non-epileptic intracranial recordings. *Brain Topogr.* **28**, 172–183 (2015).

43. C.-Y. Cheng, M.-H. Mao, Photo-stability and time-resolved photoluminescence study of colloidal CdSe/ZnS quantum dots passivated in Al_2O_3 using atomic layer deposition. *J. Appl. Phys.* **120**, 083103 (2016).

44. C. Carrillo-Carrión, S. Cárdenas, B. M. Simonet, M. Valcárcel, Quantum dots luminescence enhancement due to illumination with UV/Vis light. *Chem. Commun.* 5214–5226 (2009).

45. L. Muller, G. Piantoni, D. Koller, S. S. Cash, E. Halgren, T. J. Sejnowski, Rotating waves during human sleep spindles organize global patterns of activity that repeat precisely through the night. *eLife* **5**, e17267 (2016).

Science Translational Medicine

AAAS

Supplementary Materials for

An electroencephalogram microdisplay to visualize neuronal activity on the brain surface

Youngbin Tchoe *et al.*

Corresponding author: Shadi A. Dayeh, sdayeh@eng.ucsd.edu

Sci. Transl. Med. **16**, eadj7257 (2024)
DOI: 10.1126/scitranslmed.adj7257

The PDF file includes:

Materials and Methods
Figs. S1 to S14
Tables S1 and S2
Legends for movies S1 to S7
References (*43–45*)

Other Supplementary Material for this manuscript includes the following:

Data file S1
Movies S1 to S7
MDAR Reproducibility Checklist

Supplementary Materials and Methods

Fabrication of Brain EEG-Microdisplay

Fabrication of Flexible, Multi-Color Micro-LED Arrays

A monolithic, scalable process was developed for the fabrication of flexible GaN micro-LED arrays on 6-inch engineered substrate. The process leveraged on the low-defect density GaN epitaxially grown on a newly commercialized Qromis® Substrate Technology™ (QST) based on polycrystalline AlN (poly-AlN) with matched thermal expansion coefficient (GaN-on-QST) (Fig. S1A). An 10-µm-thick GaN epitaxial layer grown on Si(111)/SiO$_2$/poly-AlN consisted of p-type GaN (150 nm), InGaN/GaN multiple quantum wells, and n-type GaN layers (Fig. S1B).

Micro-LED die was designed to have circular shape to minimize the sharp corners to minimize the potential mechanical damage on the biological tissues. To build a working LED, ohmic contacts to p- and n-type GaN layers were first formed. p-type ohmic contact was prepared by treating the surface of p-type GaN with aqua regia for 5 min and consecutively depositing Cr/Au (10/10 nm) layers [Ref: Cr/Au ohmic contact with p-GaN]. To expose the n-type GaN, GaN layer was etched through BCl$_3$/Cl$_2$ reactive ion etching (RIE) (Oxford Plasmalab80) to expose n-type GaN layer. The exposed n-type GaN was cleaned by diluted HCl and Cr/Au (10/100 nm) contacts were selectively deposited on n-type GaN layer. Individual dies were defined by doing 10 µm deep isolation etching through a thick SiO$_2$ mask (4 µm) using inductively coupled plasma reactive ion etcher (ICP-RIE, Trion). Circular array of SiO$_2$ masking layer were formed by plasma enhanced chemical vapor deposition (PECVD, Oxford) followed by ICP-RIE patterning of SiO$_2$ through the Cr mask (200 nm).

A 5µm polyimide layer (HD2611, HD Microsystems) was coated on the substrate through 1h 350°C curing process in a Carbolite Oven. Via holes to the LED contacts and perfusion holes

were patterned (MLA150, Heidelberg) and etched (ICP-RIE, Trion) by a 100nm sputtered Ti mask (Denton Discovery 18). Then we sputtered Cr/Au (50/500nm) metal leads on this polyimide layer to form the connection to all p contacts of LEDs. A similar round of process was done including second polyimide layer deposition, via holes to the 1st metal leads and perfusion holes etching, and the metal leads deposition connecting all n contacts of LEDs. A third polyimide layer was deposited to passivate the metal leads, followed by via holes etching to expose the metal connection area. Different devices on the substrate were lifted-off in Buffered Oxide Etchant solution in two days. After lift-off process the Si layer on the back side of individual device was removed through XeF_2 Etcher (Xactix).

Fabrication of PtNRGrids

The fabrication process of Brain EEG-Microdisplay involved creating PtNRGrids with 1024 channels that were specifically designed to match the dimensions of micro-LED arrays. The process starts with using a polished and cleaned soda lime glass plate with dimensions of 7" × 7" × 0.06" as the substrate. A 3.7-μm-thick-parylene C layer is then coated on the glass substrate using a parylene deposition system (Specialty Coating Systems 2010 Labcoter), and metal leads are formed on the parylene C layers by lithography, descum, metal deposition, and lift-off process using micro-fabrication tools such as maskless photolithography system (Heidelberg MLA150), UV flood exposure system (DYMAX), plasma etcher (Oxford Plasmalab80), and e-beam evaporator (Temescal). The metal leads are composed of Cr/Au/Cr/Au (10/250/10/250 nm) formed by two cycles of patterning, deposition, and lift-off steps. A PtAg alloy is formed on individual recording sites by photolithography (Heidelberg MLA150), descum (Oxford Plasmalab80), and PtAg alloy co-sputtering (Denton Discovery 18). A Ti capping layer is deposited on top of PtAg

alloys to prevent oxidation during the following processes. After depositing the second parylene C layer (3 μm) to conformally cover all the metal leads and PtAg alloys, via holes and electrode outline etching were performed through a patterned Ti hard mask using a reactive ion etching process (Oxford Plasmalab80). The electrodes are lifted-off from the substrate and de-alloyed on the surface of 60°C nitric acid to form the non-toxic platinum nanorods (PtNRs) with low electrochemical impedance. More detailed fabrication processes and characteristics of PtNRGrids could be found elsewhere.(*21*)

Bonding and Assembly of Brain EEG-Microdisplay

The flexible μLED was connector to the LED driver electronics through a flexible printed circuit board (FPCB) and connectors. A selectively-deposited silver epoxy (8331, MG Chemicals)-based bump bonding was used to make reliable bonding interface between the thin μLED layer and customized FPCB. For the multicolor applications, red and green indium phosphide/zinc sulfide (InP/ZnS) quantum dot color conversion (QDCC) inks (Mesolight) were printed on top of the GaN dies through ink-jet material printer (Fujifilm Dimatrix 2850). InP/ZnS quantum dots were selected because they have lower potential toxicity compared to other types of quantum dots. [Ref: Brunetti, Virgilio, et al. "InP/ZnS as a safer alternative to CdSe/ZnS core/shell quantum dots: in vitro and in vivo toxicity assessment." Nanoscale 5.1 (2013): 307-317.] A 50-nm-thick Al_2O_3 passivation layer was deposited on the QDCC-printed devices using atomic layer deposition (Beneq TFS200) to minimize the moisture or oxygen exposure of the QDCC ink that may degrade the quantum efficiency of QDCC ink over time.(*44*) A 3.3-μm-thick Parylene C layer was then coated (Specialty Coating Systems 2010 Labcoter) to further passivate the device to be used in wet

environment such as brain surface. The QDCC ink was then photo-activated by UV exposure under an inert nitrogen environment to enhance the luminescence efficiency.(*45*)

To bond the PtNRGrids to the extender PCB, a selectively-applied silver epoxy (MG Chemicals 8331) was used on the PCB footprints. A stencil mask made of silicone adhesive PET tape (Advanced Polymer Tape) with laser-cut holes was used to apply the silver epoxy selectively onto the PCB footprints. The PtNRGrid was temporarily placed on a clear plastic film (Steriking)/glass plate and micro-aligned with and pressed against the extender PCB with silver epoxy bonding bumps. They were then cured on a 75°C hotplate for 15 minutes under 5-10 N force to ensure complete curing of the silver epoxy and establish electrical connections across all bonding contacts. The electrically bonded PtNRGrid was released from the glass plate, and the electrodes were characterized on a benchtop. Before bonding, the PCB edge was ground and smoothed to minimize potential damage to the thin metal leads in parylene C films.

To create the Brain EEG-Microdisplay, the PtNRGrids were assembled with a flexible µLED array. Two separate grids with matching dimensions were precisely aligned using micro-alignment stages with four-axis degrees of freedom. Once the individual µLED dies and PtNR recording sites were aligned, a small amount of photoresist (AZ5214E-IR) was applied to the 'neck' part of the µLED array and PtNRGrids through holes prepared in the µLED array (see red arrows in Fig. 1C). This held the two thin and flexible grids together (Fig. 1C) with an added feature that the µLED layer could be lifted-off from the PtNRGrids when needed. For the 32mm x 32mm Brain EEG-Microdisplay, the perfusion hole arrays in the PtNRGrids were aligned with the through hole arrays in the flexible µLED array. The through hole arrays (0.5 mm diameter, 1 mm pitch) in the Brain EEG-Microdisplay enabled Ojemann probe to directly stimulate the cortical surface through the grid. The yield of PtNRGrid and the Brain-iEEG-Microdisplay on average have 95% and 90%,

respectively. The best yields achieved for PtNRGrid and the Brain iEEG-Microdisplay were 99.4% and 95%, respectively.

Electronics and Software to Drive Brain EEG-Microdisplay

Hardware to Operate Brain EEG-Microdisplay

We developed the ORB1024_V1, an acquisition board that utilizes Intan Technologies' RHD2164 chipset, to record from up to 1024 channels concurrently, with a maximum of 30 kilo-samples per second (ksps) per channel. The board consists of 16 RHD2164 chips to amplify and digitize the brain signals, LGA1155 CPU socket that connects to our electrode arrays, and Omnetics 12-pin connectors that interface with an off-the-shelf 1024-channel Intan RHD recording controller. With the ORB1024_V1, we can connect our flexible electrodes array and digitize the 1024-channel analog brain signals robustly. Using the Intan RHD recording controller, we set the sampling rate of the RHD2164 chips as 20 ksps and recorded the ECoG signals with a data rate of around 2.4 GB/min. The recorded streaming data is transmitted from the recording controller to a host computer via the USB interface.

Fig. S5A depicts the μLED + μECoG feedback system, which comprises the recording station mentioned above, a host computer, and μLED subsystem with a mechanical toggle switch and an external impedance analyzer. The recording station records neural activity and feeds it to the μLED subsystem to map the neural activity onto the μLED array. As shown in Fig. S5B and S5(C), the LED driver board has four LED driver chips (IS31FL3741A, Lumissil) that can support driving the 32 × 32 single-color GaN μLED array with a voltage level of 5 V and an average current of 3.75 mA. Also, the board includes the MCU, Teensy 4.1, to configure the LED driver chips through the 1 MHz I2C interface and to supply power through the USB interface. For the

dual-color Brain-iEEG-microdisplay, two LED driver boards were used and controlled individually via the host computer.

Our μLED subsystem supports three operation modes: normal mode, impedance measurement mode, and hardware shutdown mode. In normal mode, the host computer receives 20 kSps recorded brain waves through USB_0, and the Qt software processes the data and sends a series of control bits to the μLED subsystem through USB_1. The MCU transforms the USB-formatted data into the I2C format to program the LED driver chips, resulting in a change of the LED pattern. Through an iterative process of updating the LED driver chips based on recorded brain waves, the μLED subsystem can provide video-rate visualization. To ensure the safety of the brain and the surrounding tissue, the μLED subsystem switches to impedance measurement mode every 10 seconds in normal mode by setting MODE_SEL low. In impedance measurement mode, the μLED subsystem keeps track of the leakage current on the brain and the tissue by measuring the impedance between the μLED array and a reference node. As the reference node, a needle is connected with the ground of the electronic system and inserted into the tissue (Fig. S5C). Upon entering impedance measurement mode, the μLED driver board electrically ties up all the column and row control lines of the LED matrix into a single node by changing the active channel of the FET multiplexers. After the multiplexers are set, the impedance analyzer inputs the current over the LED array and measures the impedance between the LED matrix and the reference needle. In this work, additional single Intan chipset and its controller are used as an external impedance analyzer. If the measured impedance at 1 kHz is higher than 100 kOhm, the system goes back to normal mode by setting MODE_SEL high. However, if the measured impedance gets lower than 100 kOhm, the μLED subsystem enters shutdown mode, which power down the μLED driver chips, to prevent damage to the brain. The system also includes a manual toggle switch that enables

to enter shutdown mode in unexpected situations. The overall flow chart of the μLED subsystem operations is shown in Fig. S5D.

Soak test of Brain EEG-Microdisplay

An electrical safety assessment under moist environment would be crucial for the clinical translation of Brain EEG-Microdisplay and its applicability beyond the acute demonstration provided in this study. Utilizing the impedance monitoring hardware set up described in Fig. S5C, we conducted a soak test of the Brain-iEEG-microdisplay by immersing the device in saline solution for one week. Throughout the week, the device remained continuously soaked in saline, with impedance measurements taken daily during a 10 min session with all LEDs activated. We found that the device's impedance stayed nearly unchanged throughout the week, with no signs of decrease (Fig. S12). The minor fluctuations in impedance readings may stem from replenishing the saline solution to compensate for its natural evaporation and from changes in the positioning of the ground/reference needle electrode within the saline during this replenishment process. This consistency in impedance over one week soak test underscores the device's durability in a moist environment.

Near real-time Data Processing Software of Brain EEG-Microdisplay

The brain data recorded with the 1024-channel PtNRGrids were processed in near real-time to instantaneously display the cortical activity on the microdisplay. This near real-time data processing method was used to display the epileptiform activities (Fig. 5) and extent of electrical stimulation (Fig. 4) from the surface of the brain. To achieve this, the Intan Technologies' C++/Qt open source RHD Recording Controller software (Version 2.08) was customized to perform high and low pass filtering and spatial mapping of RMS potentials on all channels. The computer

received 25 ms of data packets containing 1024 channels from Intan recording controller. The 25 ms data packet was bandpass filtered in 10-59 Hz frequency window, and root-mean-square (RMS) value of filtered data was calculated for individual channels to generate a single frame of spatial map of the RMS potentials. These RMS mapping data were displayed on the processing computer screen, and serial communication was used to send the spatial mapping information to the microdisplay via a Teensy 4.1 microcontroller. The resulting refresh rate of the microdisplay was 40 Hz.

Trial averaging was used to show the M1/S1 boundary and the localized high gamma activities of the animal under repeated electrical or mechanical sensory inputs. A sensory input to the animal was configured to send a time-locked TTL signal to the Intan recording controller. Once a TTL signal was captured, an evoked response waveform typically between 0 to 100 ms post-stimulus was stored in the memory which waveforms were updated by trial averaging with the additional inputs of evoked responses. The typical post-stimulus time range used for RMS mapping in the Brain EEG-Microdisplay was configured to be between 18 and 22 ms. The software had a user-input feature that allowed the user to select the post-stimulus time range for calculating the RMS mapping.

To ensure a seamless image on the microdisplay, impedance measurements were performed to screen out channels with high impedance (>100 kΩ at 1 kHz) that showed poor electrochemical impedance, causing high-amplitude noise and large RMS potential. This was necessary to avoid distortion of the actual brain activities. The RMS potential values of the nearest neighboring channels with good impedance (<100 kΩ at 1 kHz) were then used to fill in the RMS potential value on the high-impedance channels, enabling a continuous display of the cortical activity on the microdisplay.

Noise contribution of LED to the ECoG recording

The close proximity of the μLED system and μECoG grid caused interference between the two systems, resulting in high-frequency noise being added to the ECoG signals once the μLED system was powered on. This interference was due to the microdisplay being driven by high-frequency 5V square pulses; even when all the LEDs are not emitting light, the LED driver (Lumissil IS31FL3741A) sends 5V pulses sequentially to all the rows (n-contact) and columns (p-contact), setting the net bias voltage to 0. The noise power spectral density plots before and after turning on the LED system (Fig. S13) show multiple discrete peaks starting from 98.63 Hz and their harmonics at higher frequencies. For the near real-time display of cortical activities, we applied a band pass filtering below 90 Hz (typically between 10 and 59 Hz) to the ECoG signals which effectively filtered out the artifactual noise caused by the LED system.

For the trial averaged high gamma activities, although the selected frequency window of 70-190 Hz included some noise peaks from the LED, this noisy signal averaged out with increasing number of trials. To achieve a lower background noise level during the HGA mapping, another strategy was to use a switch that could power on and off all the LED driving chips. The switch was used to turn off the LEDs while recording the brain activity in response to the sensory tasks. The recorded responses were averaged over multiple trials. After the sensory task was completed, the high gamma activity (HGA) map was displayed by turning on the LEDs.

Offline Data Analysis

Together with the near real-time processing to display cortical activities on the brain, the ECoG signals from 1024 channels were recorded for offline analysis. Individual recording channels were mapped to the individual spatial coordinates on the PtNRGrids, and this mapping

was tabulated in a spreadsheet for each electrode type. This allowed us to spatially display waveforms, RMS potentials, and impedance magnitude using the recorded data. To ensure accuracy of the analysis, channels with an *in vivo* impedance magnitude above 100 kΩ at 1 kHz were excluded from analysis, as they usually showed a response that was artificially large and were more susceptible to noise. Additionally, neighboring channels with very low impedance magnitude (< 1 kΩ at 1 kHz) were evaluated as potentially shorted channels and were excluded from the offline analysis. Furthermore, all recorded signals (unless explicitly specified as "raw") underwent processing to eliminate 60 Hz and their noise harmonics using digital notch filters.

For the M1/S1 sensory boundary localization, signals were digitally filtered in the frequency window of 10-3000 Hz using a Butterworth 4th order filter with MATLAB's "filtfilt" function. No re-referencing was used since this could potentially cause an undesirable offset in SSEPs. TTL pulses time-locked to the electrical stimulation of forelimb was used to determine time epochs for trial averaging (n=50) the SSEPs.

The HGA mapping was carried out by trial averaging the raw waveforms based on the TTL pulses time-locked to the air-puff or electrical stimulation. We then re-referenced the recorded signals by subtracting the common-averaged signal across channels. The common-average was calculated either by taking the average of all the working channels or by taking the average of a few selected channels.(*21*) This effectively removed the motional artifacts, electrocardiogram, and low frequency noise. The signals were digitally filtered using a Butterworth 4th order filter under selected frequency windows of 70-190 Hz, and 50 trials were aligned and averaged based on the TTL pulses that triggered air-puff or electrical stimulation. All digital filters were implemented in Matlab using the zero-phase distortion filtering function, "filtfilt", which effectively doubled the filter order to 8. The amplitude of the signals in each frequency window were calculated by taking

root-mean-square (RMS) of the absolute value of the Hilbert transformed signal in a 15~25 ms time window after the stimulation.

The propagating dynamics of the beta waves were calculated by taking the spatial phase gradients of the beta waves following the methods described in Rubino *et al.(42)* and Muller *et al..(46)* The signal was first filtered in beta band of 9-18Hz using a Butterworth 4th order filter with the "filtfilt" function in Matlab. The phase angle of the beta wave for each channel was calculated by taking the inverse tangent of the imaginary part over the real part of Hilbert transformed data, and the phase was unwrapped over time. The propagation directions of the beta waves calculated from the spatial phase gradient were represented as a vector field and streamlines, were used to visualize the long-range propagation directions of the waves. The streamlines were plotted using the streamline function in Matlab with a default setting.

We used offline analyses to detect interictal discharges (IIDs) using an automatic IID detection algorithm (version v21, default settings except -h at 60; http://isarg.fel.cvut.cz) (*43*) The automatic IED detection algorithm adaptively models distributions of signal envelopes to discriminate IIDs from intracranial recordings. (*43*)

Pig Experiments

Pig Models and Task Information

Table S1 summarizes the pig models, devices, and task information.

Anesthesia and Pre-operative Preparation of Pigs

All procedures for the pig experiment were approved by the UCSD Institutional Animal Care and Use Committee under protocol S19030. The pre-operative medication included a cocktail of Ketamine, Midazolam and Atropine - administered IM. An 18G catheter was placed into an ear

vein and tracheal intubation was performed with the aid of a laryngoscope. A cuffed endotracheal tube was placed, secured, and connected to an anesthesia machine equipped with a charcoal canister as a scavenger. Mechanical ventilation was initiated with a tidal volume set at approx. 10 cc/kg at a rate of 8-14 breaths per minute and lactated ringers or saline were infused through an intravenous line at 5-10 ml/kg/hr. Isoflurane anesthesia was maintained using 1-3% isoflurane in 100% oxygen. The animal's depth of anesthesia was continuously monitored by observation of vital signs and the animal's reflex responses. Vital signs including HR, RR, SPO_2, temperature, and $ETCO_2$ were monitored and recorded every 15 minutes. The monitored reflexes included the palpebral and pedal responses, as well as jaw tone strength. End tidal CO_2 ($ETCO_2$) was monitored and maintained between 35-45 mmHg. A fluid warmer and/or Bair Hugger were utilized in all studies to maintain normal body temperature. Clipping of the hair was performed at the surgical sites. Once the brain EEG-microdisplay was placed on the cortex, the animal was transitioned from isoflurane to IV propofol anesthesia for the remainder of the experiment. During the analysis of epileptiform discharges, a paralytic agent (vecuronium) was readily available in case of a severe motor seizure response in the animal. Only minor motor responses were observed in response to the epileptogenic agents and vecuronium administration was unnecessary. In one animal, vecuronium was administered to reduce shivering artifact that was unresponsive to adequate anesthesia and temperature control.

Surgical Procedures for Pig Craniotomy and Brain EEG-Microdisplay Implantation

The surgical site was centered over the motor cortex of the frontal lobe and somatosensory cortex of the parietal lobe. Once anesthetized, the animal was mounted into a stereotaxic frame. After immobilization, a skin incision measuring 2-4 inches in length was made. The skull was then

exposed using a chisel and retractors, and a bilateral craniotomy was performed using a neurosurgical drill. The skull was removed to create a window approximately 40 mm × 40 mm. The dura underlying the skull was cut open except the dura near the midline. Once exposed, the cortical surface was hydrated throughout the experiment with saline. A brain EEG-microdisplay was then placed on the surface of the exposed cortex.

Sensory Tasks in Pig Experiments

Electrical stimulation of pig was carried out with 12 mm twisted-pair subdermal needles (Natus) and Intan RHS recording and stimulation system. The subdermal needles were poked into the skin by 12 mm with typically 2 mm separation between the pair of needles. Biphasic current pulses with amplitude of 2 or 10 mA and pulse width of 1.0 ms were delivered to the bipolar needles to stimulate various parts of the pig. The parts we stimulated include forelimbs, snout, cheek, and tongue. Since the maximum current level that could be generated from a single channel in Intan RHS system was around 2.5 mA, we shorted 5 channels and connected them to a single needle and sent time-locked current pulses to 5 channels at once to achieve 10 mA. The other needle was connected to the ground/reference pin in the RHS headstage.

Snout and tongue of pigs were locally stimulated with an air-puff stimulator using the Pneumatic PicoPump (WPI, PV830). Air-puff was delivered through a 1 mm diameter glass microcapillary tube with a pressure of 40 psi. Each air-puff stimulation position was stimulated 50 times, once every 1 s.

Both the air-puff and electrical stimulation were time locked to the recording system by sending TTL signals to both the stimulator and the Intan recording controller.

Direct Electrical Stimulation of Pig Brain

Pig brain was electrically stimulated at the surface or at depth using clinical stimulators. A Ojemann probe was used to deliver 3 mA biphasic pulses of current at 50 Hz with variable stimulation time ranging from 0.1 to 2 s. Multiple positions on the pig's cortical surface were stimulated either through or around the Brain-iEEG microdisplay. 16 channels stereoelectroencephalography (sEEG) electrode (PMT Corp.) with contact spacing of 6 mm and diameter of 0.8 mm were manually inserted into the depth of the pig brain by 6 cm. Intan RHS system was used to deliver biphasic current pulses of 1~10 mA (0.5 ms positive, 0.5 ms negative) to the adjacent channels on the sEEG electrode. To generate a 10 mA current level, we combined the output of 5 channels in the Intan RHS system by shorting 5 channels to a single needle.

Epilepsy Pig Model

Epileptic discharges were acutely introduced on the pig brain using epileptic discharge inducing drugs approved under protocol S19030. We used three different epileptic discharge inducing drugs with different application methods on four different pigs including i) topical application of crystals of 1(S),9(R)-(-)-bicuculline methiodide (BIC, Sigma-Aldrich 14343) on the pig's cortical surface, or subcortical injection of ii) 10 µL, 100 mM 4-aminopyridine (4-AP, Sigma-Aldrich A78403) solution or iii) 10 µL, 100 mM benzyl-penicillin (Pen-G, Sigma-Aldrich 13752) solution. The drugs were reapplied every 15 min for a total of 3 applications to keep up the efficacy of the effect. All three drugs induced clear epileptic discharges, while the efficacy, amplitude, and spatial distribution of epileptic discharges varied between the three drugs studied. Of the three drugs, BIC produced the highest amplitude epileptiform activity. Notably, controlling the amount of BIC was challenging given its crystalline form which may have led to an overdosing of BIC

compared to the other drugs. During our study on anesthetized pigs, we observed mild motor seizure activity near the snout of one pig (Fig. S12), while we did not observe any other motor seizure activity in the other pigs after careful full body observation.

Histology of the Pig Brain

The brain under the iEEG-microdisplay was resected and immediately immersion fixed in 4% PFA for 24 hours before being transferred to 30% sucrose. The brain was blocked and sectioned at 50 μm on a cryostat and slices were stored in PBS + 0.01% Sodium Azide before further processing. Control and experimental sections from each block were processed in the same well to limit variability. Slices were washed for 2 hours in PBS and blocked for 1 hour in 5% normal goat serum (Jackson Immunoresearch, PA). Sections were incubated with Neurotrace 640/660 (1:50, Thermo Fisher Scientific Cat# N21483) for 30 minutes. Sections were washed for 2 hours in PBS before being mounted and coverslipped with Prolong Gold Antifade Reagent with DAPI. Sections were imaged on a Zeiss Apotome2.

Rat Experiments

Rat Models and Task Information

Table S2 summarizes the rat models, devices, and task information.

Surgical Procedures of Anesthetized Rat Craniotomy

All procedures for the rat experiment were approved by the UCSD Institutional Animal Care and Use Committee under protocol S16020. Male Sprague Dawley rats (10-18 weeks of age) from Charles River were sedated with 3-4% isoflurane and fixed in a stereotaxic frame (Kopf Instruments). Once stable, rats were reduced to 3% isoflurane for maintenance, while monitoring

heart rate and blood oxygen levels (Mouse Stat Jr, Kent Scientific). Prior to the craniotomy, contralateral side individual whiskers that were to be stimulated were colored with Sharpies to easily distinguish them in the air-puff stimulation experiment, and the remaining whiskers were trimmed off. A craniotomy was made on the right skull 1 cm lateral and 2 cm posterior from the bregma, exposing the somatosensory (including barrel) cortex, over the right motor cortex. The dura was carefully opened and retracted from the brain, and a small piece of saline-soaked gauze was placed over the brain until the implant was ready. Once the craniotomy was complete, the rat was transitioned from isoflurane to ketamine/xylazine (100 mg/kg ketamine / 10 mg/kg xylazine) and re-dosed every 20-30 min for the duration of the experiment. Temperature, heart rate, and oxygen concentrations were monitored for the entirety of the experiment to ensure adequate anesthesia.

Sensory Stimulation Tasks on the Rats

The typical size of the craniotomy was $6 \times 6\text{mm}^2$, and the $5 \times 5\text{mm}^2$ Brain-iEEG microdisplay was implanted covering nearly the entire exposed area of the brain. The reference needle electrode was implanted on the scalp of the rat just next to the craniotomy, and ground was typically connected to a surrounding faraday cage or stereotaxis frame. Individual whiskers were stimulated with an air-puff stimulator using the Pneumatic PicoPump (WPI, PV830). Air-puff was delivered through a 1 mm diameter glass microcapillary tube with a pressure of 20 psi for single whisker stimulation and 40 psi for whole whiskers stimulations. After a 10 s baseline recording, each whisker was stimulated 50 times, once every 1 s. To minimize the chance of stimulating multiple whiskers other than the whisker of interest, whiskers were subsequently trimmed off after

each recording. The air-puff stimulations were time locked to the recording system by sending TTL signals to both the stimulator and the Intan recording controller.

Epilepsy Rat Model

Epileptic discharges were acutely introduced on the rat brain using epileptic discharge inducing drugs approved under protocol S16020. We used two different drugs with different injection methods including topical application of i) crystals of 1(S),9(R)-(-)-bicuculline methiodide (BIC, Sigma-Aldrich 14343) or ii) 50 µL, 100 mM 4-aminopyridine (4-AP, Sigma-Aldrich A78403) solution on the rat's cortical surface just next to the Brain-iEEG microdisplay. The drugs were reapplied every 15 minutes on the same spot to maintain their efficacy, with a maximum of three applications. It is worth noting that when the 4-AP solution was topically applied, it immediately spread over the entire craniotomy, while the BIC crystal in powder form, applied on the cortical surface, slowly dissolved over time on the brain. Both drugs induced clear epileptic discharges, but the response to BIC was more localized on the rat brain. This is likely due to the difference in the degree of spread of the drugs on the cortical surface. During our study on anesthetized rats, we rarely observed motor seizures despite of the huge (> 1 mV) and repetitive epileptiform discharges showing up across the rat brain.

Cortical Surface Temperature of a Rat Under LED Operation

We have characterized the cortical surface temperature of a rat under Brain-iEEG-microdisplay operation. To do this, all the 1024 µLEDs with 100 µm diameter with a pixel pitch of 0.15 mm were operated in duty cycles between 0.7 and 5.6% with the Brain-iEEG-microdisplay. (Fig. S4). Infrared (IR) imaging camera measurement showed a temperature increase of up to 6, 4,

and 2°C when all 1,024 μLEDs were turned on at duty cycles of 5.6% (maximum brightness), 2.1%, and 1.0%, respectively. At a duty cycle of 0.4% or lower, the temperature change was negligible, less than 1°C, while maintaining satisfactory brightness (Fig. S4).

Interestingly, in contrast to the surface heating observed in the rat brain, the application of μLEDs at maximum brightness on the pig brain showed no temperature rise (Fig. 1E). The clear difference in surface heating between the rat and pig brains can be attributed to differences in the density of the μLED arrays. The pig brain utilized a 2,048 micro-LED array with pitches of 0.4 - 0.5 mm, compared to the 1,024 micro-LED array with a pitch of 0.15 mm used on the rat brain. Given these differences, the heating power density on the pig brain is estimated to be only about 11% of that on the rat brain surface. Additionally, the significant disparity in body mass between pigs and rats, where pigs are approximately 150 times heavier, notably impacts heat management. This marked difference in mass enables pigs to function as a much larger heat sink. Moreover, the greater size of the pig may also contribute to considerably enhanced homeostatic regulation capabilities.
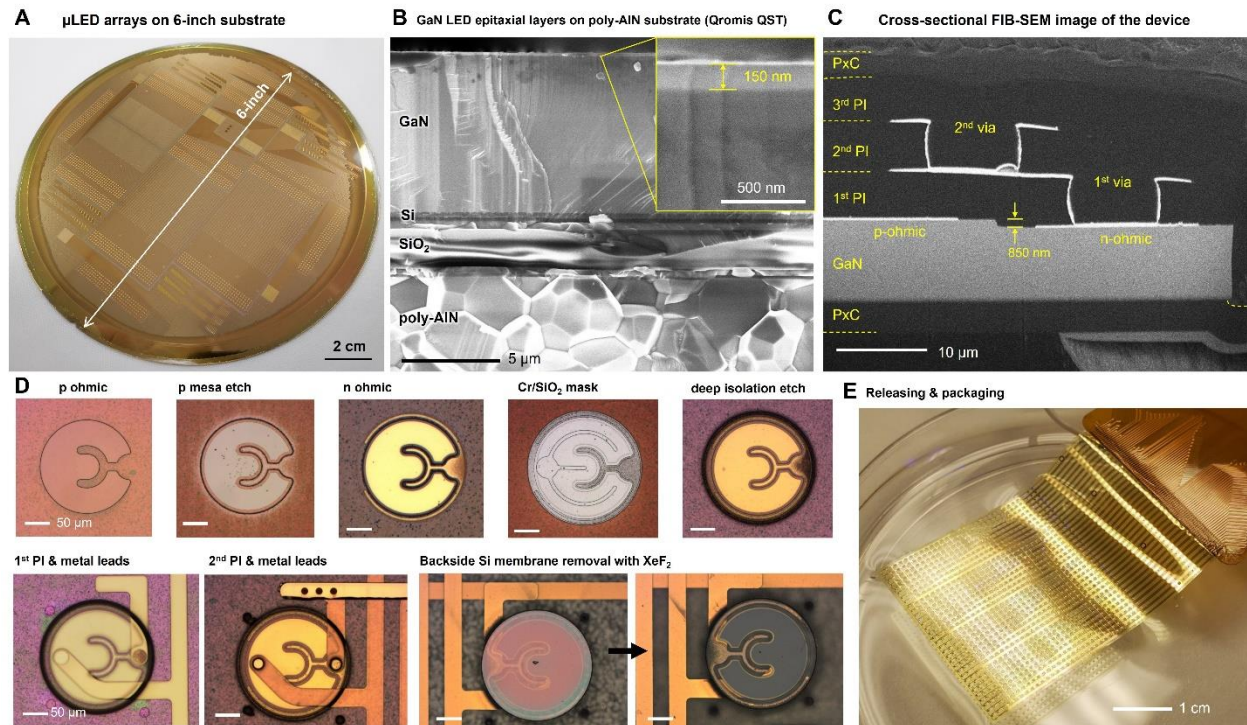
Figure S1. Microfabrication procedures of flexible μLED arrays. (A) Photo of μLEDs processed on the Qromis 6-inch QST wafer. (B) Cross-sectional SEM image of QST wafer that consist of poly-AlN substrate, SiO$_2$ intermediate layer, and GaN epitaxial layer with LED structures. 150-nm-thick p-type GaN layer is shown in the subset figure. (C) Cross-sectional FIB-SEM image of the completed μLED with GaN LED die, ohmic contact metal layers, via metallization layers, and multiple polyimide layers and parylene C layers for the crossbar array and electrical passivation. (D) OM image of the microfabrication process including ohmic metal contacts, etching, isolation etching, via metal connection, and backside Si membrane etching. (E) Released flexible μLED layer by dissolving the SiO$_2$ layer shown in (B). μLED is bonded to the FPCB by the silver epoxy bump bonding.
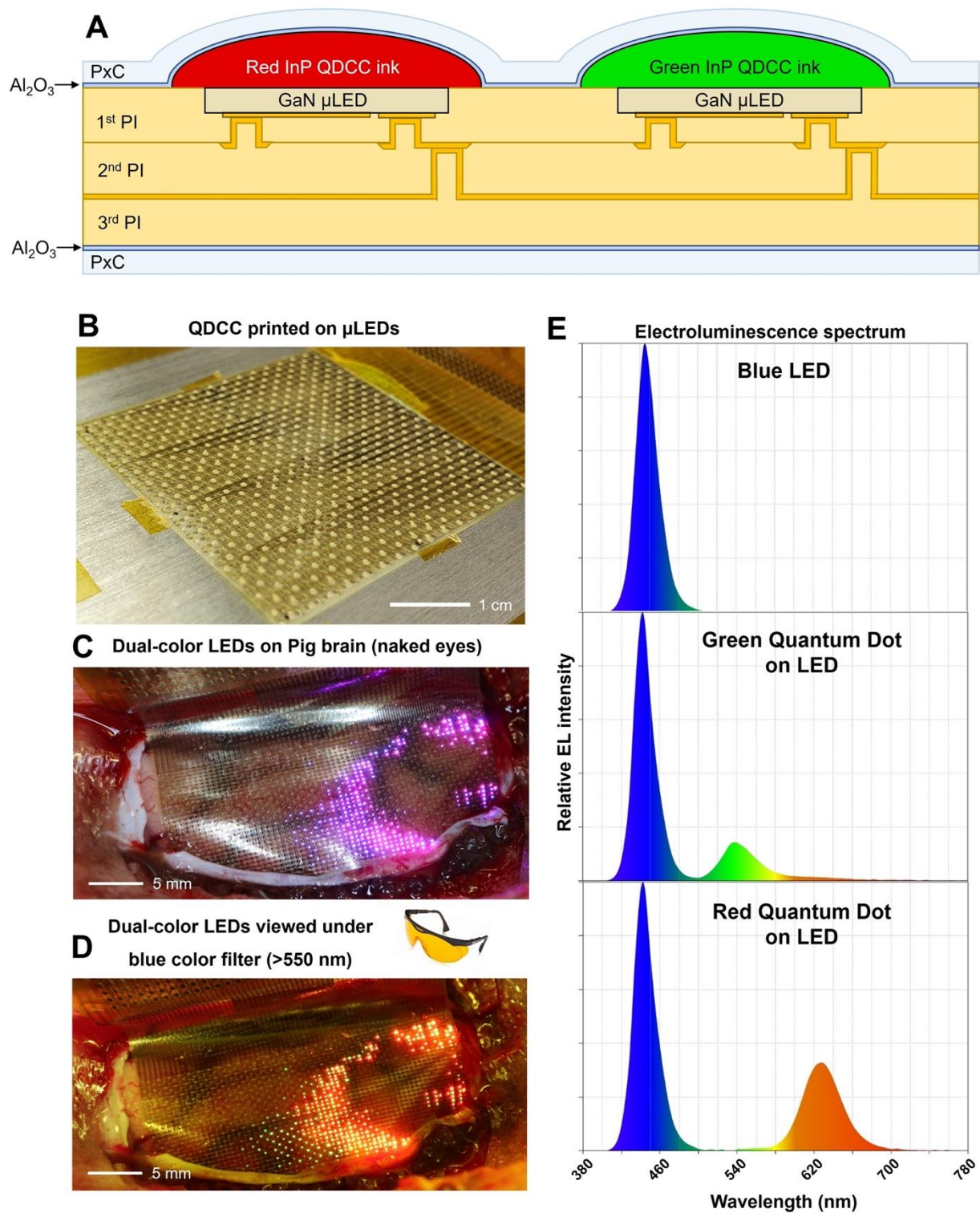
Figure S2. Multicolor LED fabrication and luminescence characteristics. (A) Schematic illustration of cross-sectional structure of µLED with red and green InP Quantum Dot Color Conversion (QDCC) inks. Schematics are not drawn to scale. (B) QDCC ink printing on the µLED array by the Dimatix DMP-2850

material printer. Dual-color LEDs on the pig brain showing the motor/sensory boundary (C) under naked eyes and (D) under 550 nm blue light blocking lens. (E) Electroluminescence spectra of blue μLED and color converted μLEDs with red and green QDCC inks. (C)-(D): Representative results are presented from 1 out of 2 pigs with unilaterally placed dual-color μLEDs (Pigl #6).
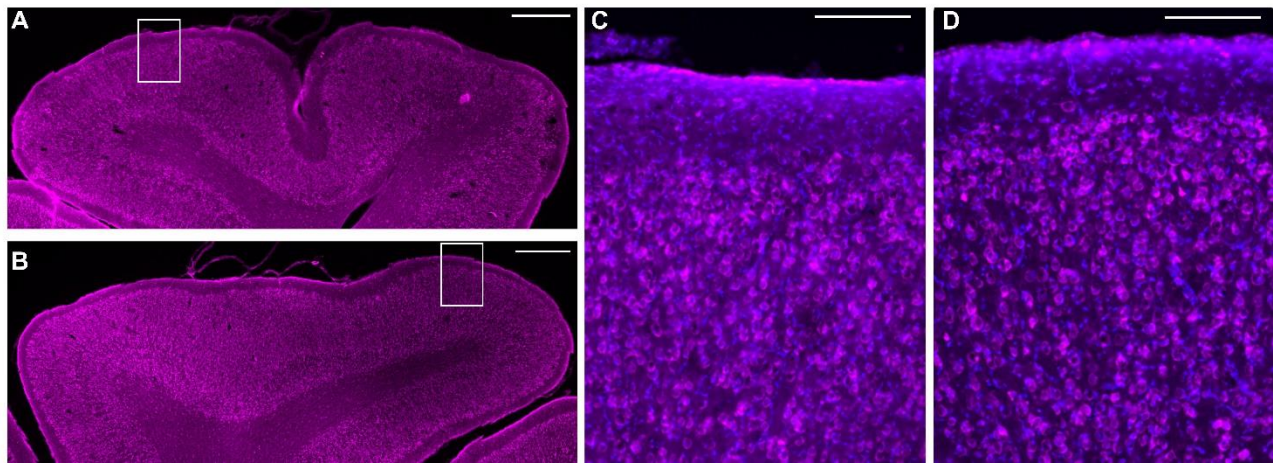
Figure S3. Representative images of the cortical surface after Brain-iEEG microdisplay recording. Tiled image of rostrum from the (A) contralateral and (B) grid side with Neurotrace (fluorescent Nissl) staining reveal intact cortical layers with no gross damage on the experimental side (Scale bar = 1 mm). Inset images from the (C) contralateral and (D) experimental demonstrates comparable Layer I thickness, neuron density, and cell morphology (Scale bar = 200 μm). (A)-(D): Representative results are presented from 1 out of 1 pig with unilaterally placed dual-color μLEDs (Pigl #6).
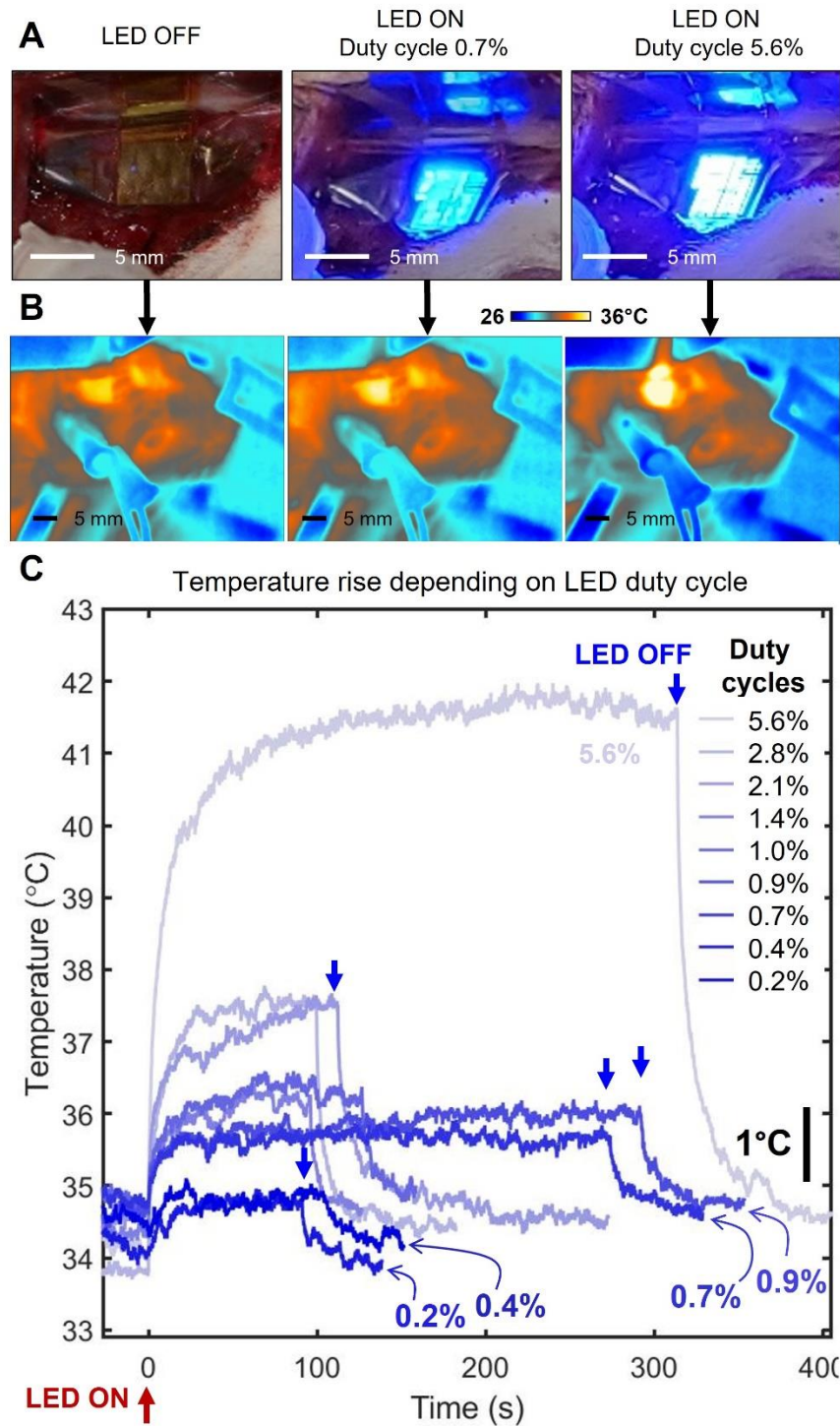
Figure S4. Cortical surface temperature of the rat brain under the LED operation. (A) Photo of μLED arrays on the brain with LEDs off and with all the LED pixels turned on at 0.7 and 5.6% duty cycles. (B) Corresponding infrared (IR) thermal images when LED was off, or ON at 0.7 and 5.6%. (C) Temperature rise and fall with LEDs turned on at different duty cycles and turned off. (A)-(C): Representative results are presented from 1 rat out of experiments on 1 rat (Rat model #4).
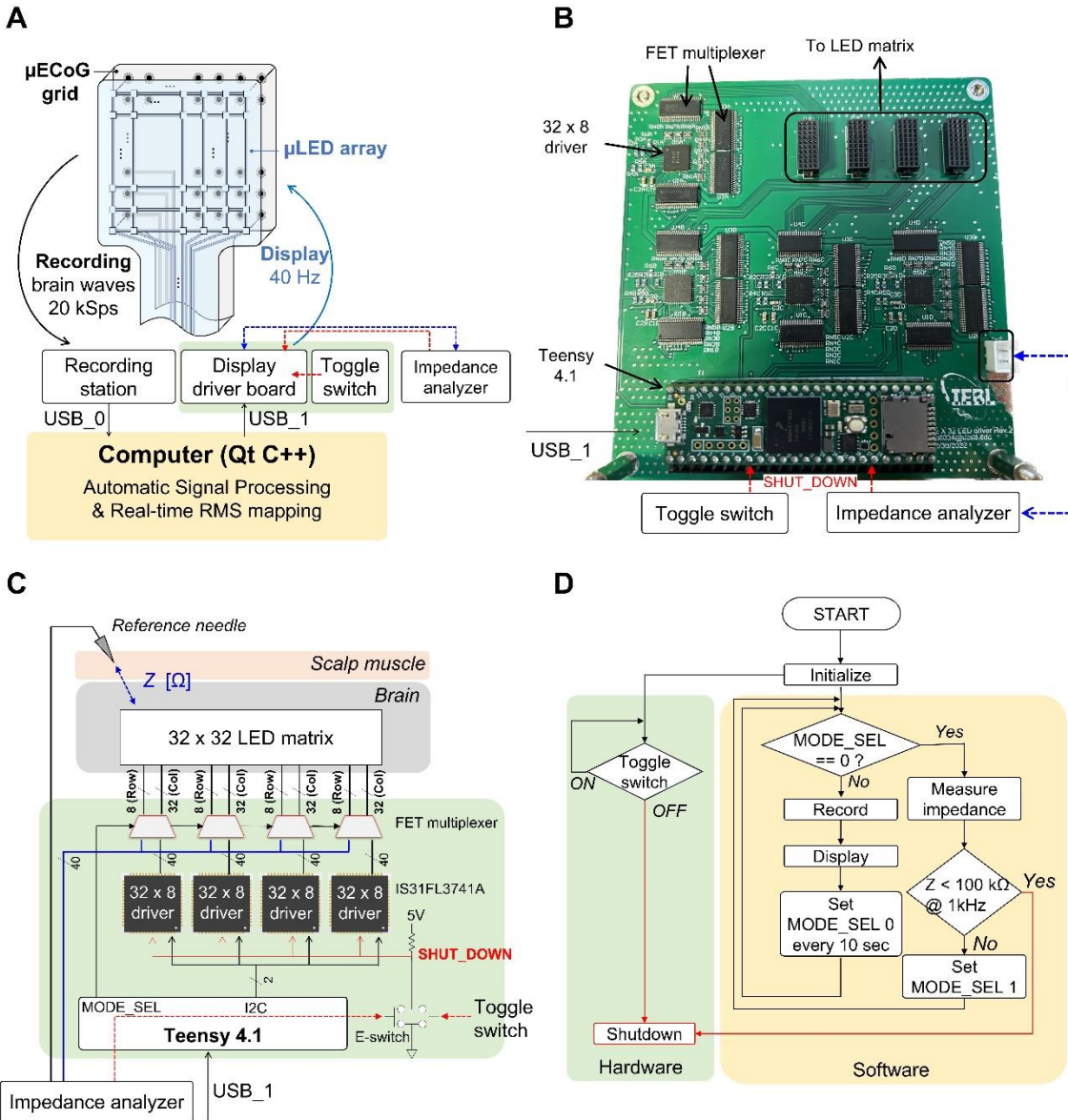
Figure S5. µLED + µECoG processing system. (A) Overall block diagram of the feedback system between the µLED and µECoG subsystem, (B) Photograph of the µLED driver board, (C) Schematic of the µLED driver system, and (D) Flow chart of the µLED controlling system.
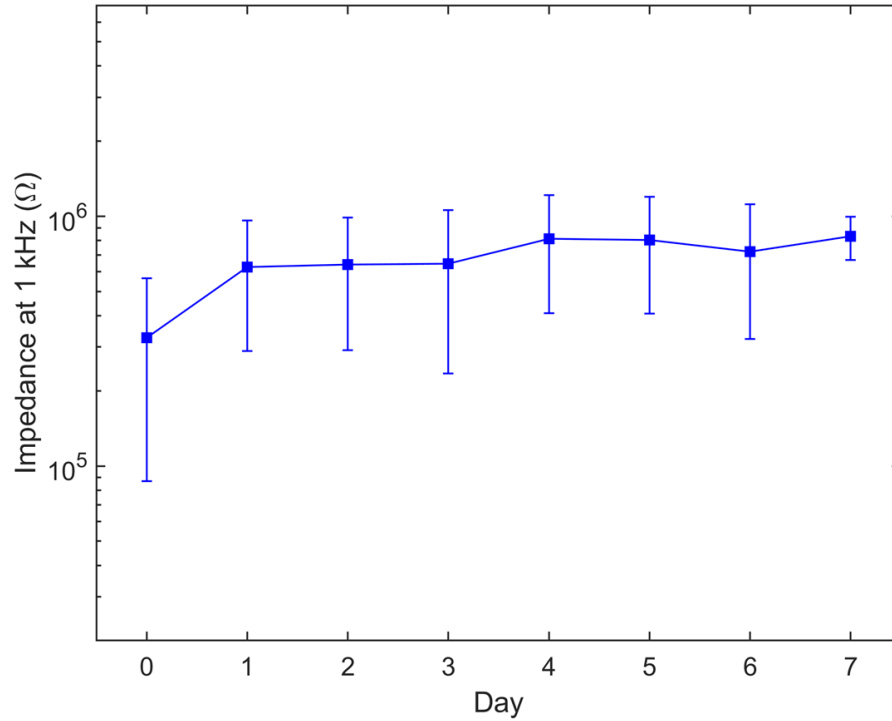
Figure S6. Evaluation of electrical safety of Brain-iEEG-microdisplay soaked in saline over 7-days. The impedance of the device was monitored with respect to saline.

Pig case Nov 16, 2022

Line depiction of FB
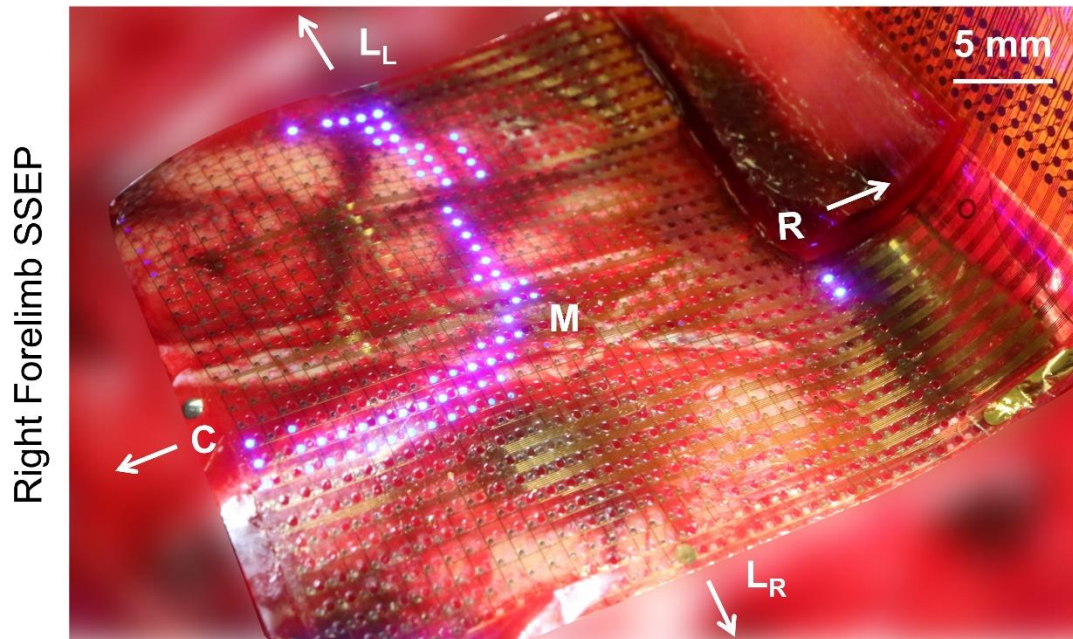
Figure S7. Real-time mapping and display of the primary somatomotor cortex (M1) and primary somatosensory cortex (S1) border on the cortical surface of the other pig brain (Pig #3).
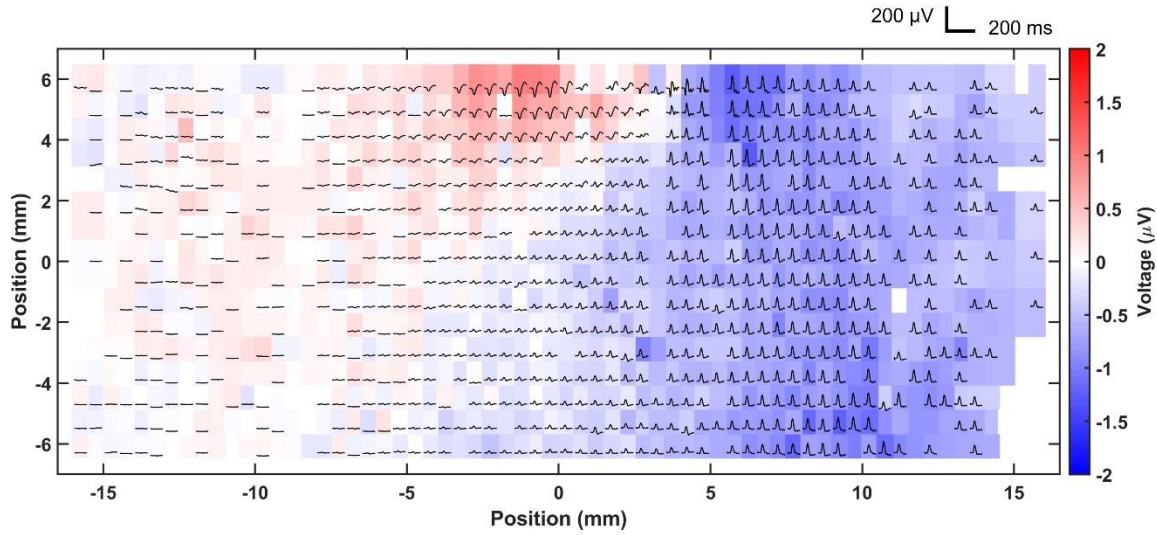
Figure S8. Offline analysis of phase reversal mapping of M1/S1 boundary on the pig brain with 13mm x 32mm brain EEG microdisplay device, corresponding to Fig. 2J.
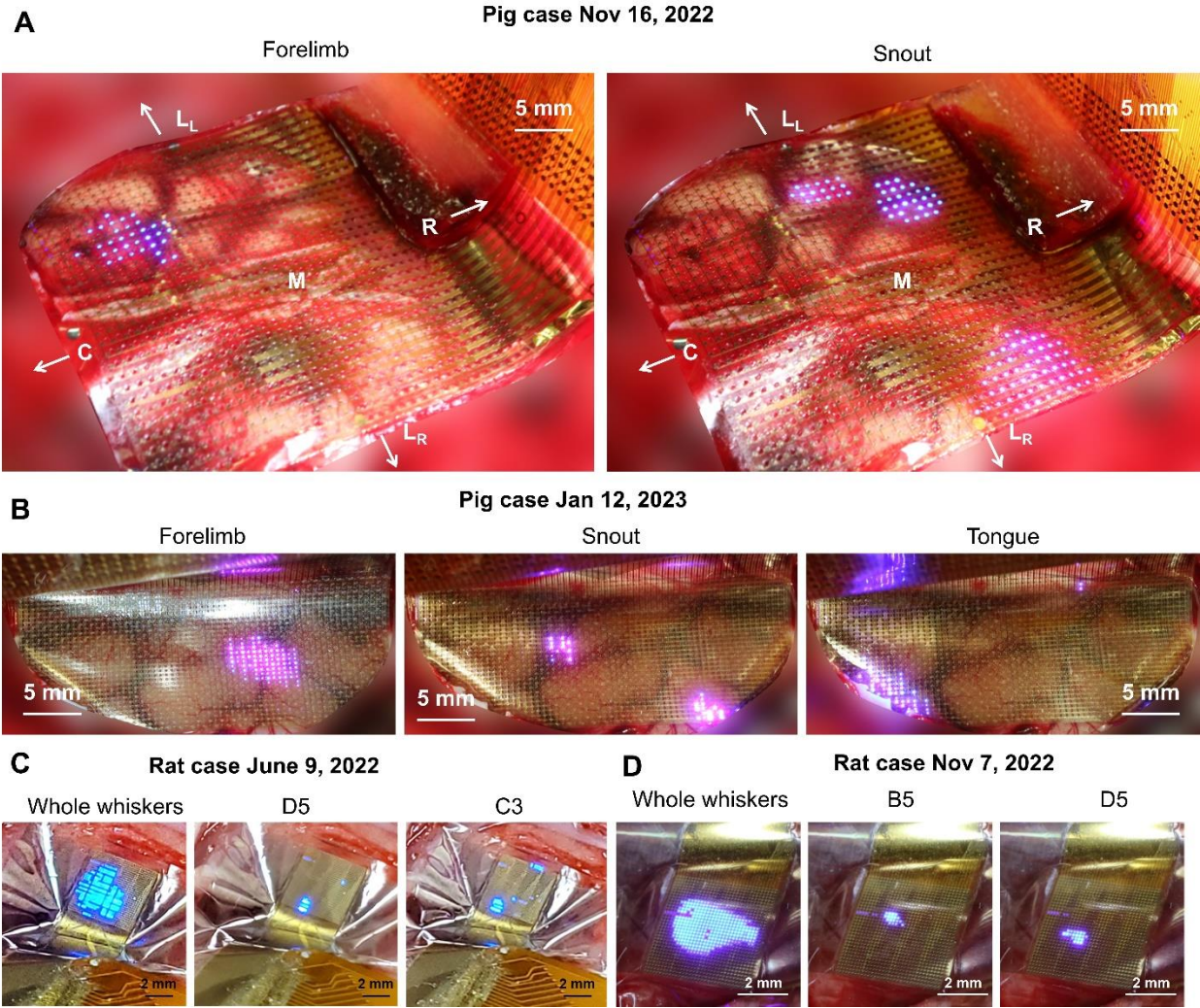
Figure S9. Sensory mapping and display on the cortical surface of other pigs' and rats' brain than those presented in the main manuscript (See data file). (A) Pig #3. (B) Pig #5. (C) Rat model #3. (D) Rat model #5.
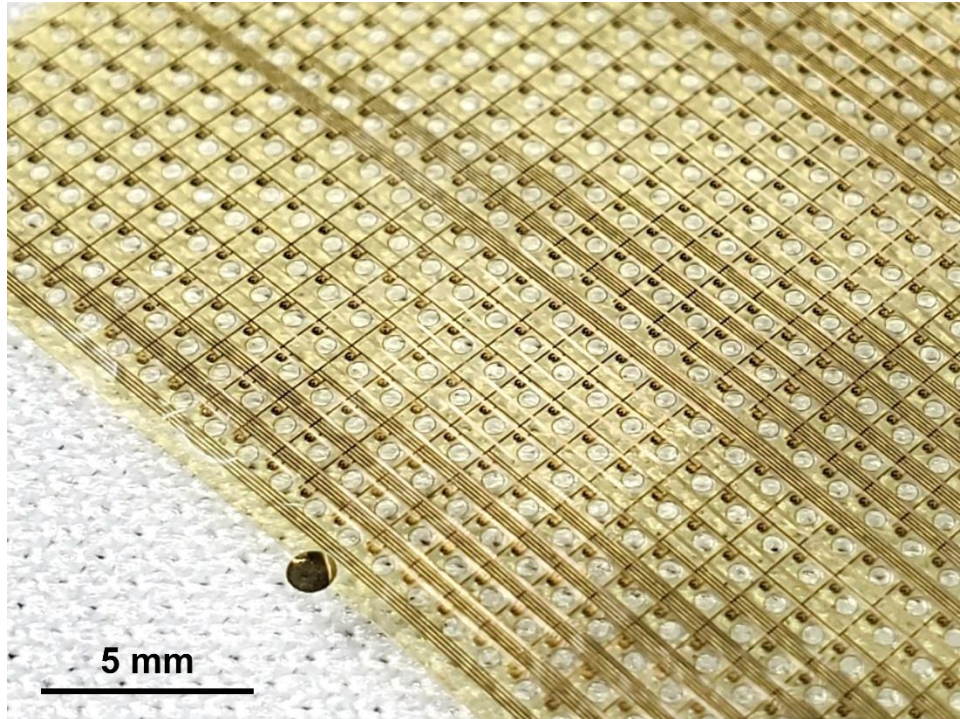
Figure S10. Perforated hole array on Brain-iEEG microdisplay that allowed through-grid direct electrical stimulation. The device is placed on a cleanroom woven polyester fabric.
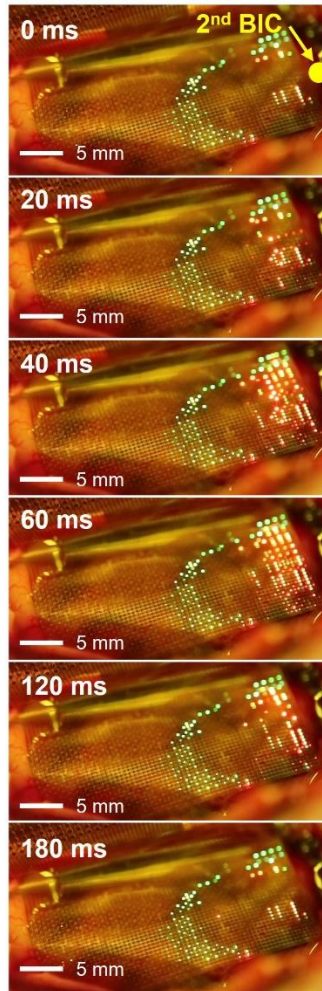
Figure S11. Effect of another BIC application on a different spot on the cortex after Fig. 5F. Series of potential maps displayed on the cortical surface (under 550 nm blue blocking lens) with 'green' color showing the motor/sensory functional boundary and 'red' color showing the online potential map of epileptiform activity under the 2nd BIC application on the cortex. New putative epileptiform activities emerged near the position of 2nd BIC dose and propagated from right to left. Representative result is presented from 1 out of 1 pig with BIC dose and unilaterally placed dual-color μLEDs (Pig1 #6).
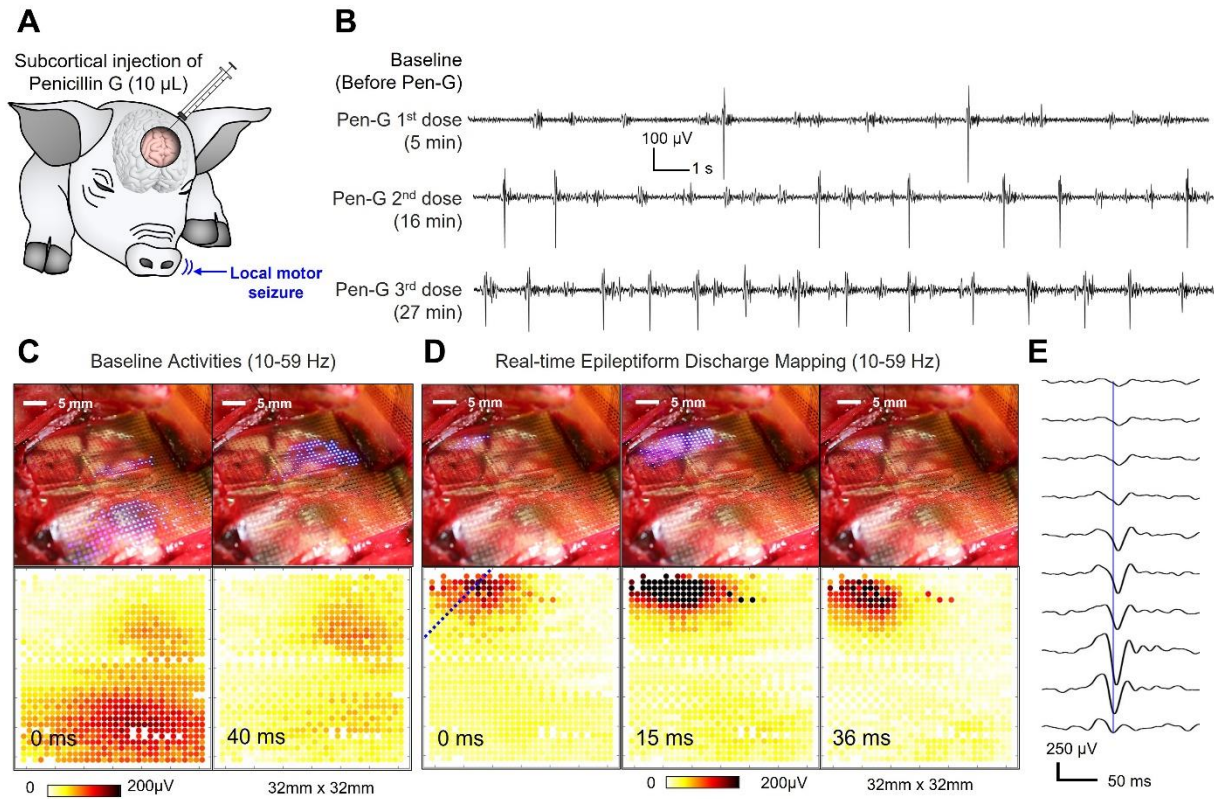
Figure S12. penicillin G (Pen-G)-induced putative epileptiform activities display on the cortical surface. (A) Schematics of evoking epileptiform activities on the pig brain by Pen-G). (B) ECoG waveforms of baseline activities before the Pen-G, and 3, 4, and 6 min after the application of Pen-G. (C) Baseline activities of brain waves visualized with LED+ECoG on pig brain and corresponding potential mapping generated by offline analysis. (D) Epileptiform activities of brain waves visualized with LED+ECoG on pig brain and corresponding potential mapping generated by offline RMS potential mapping analysis. (E) Epileptiform spike across the channels along the dotted blue line in (D). Representative result is presented from 1 out of 2 pigs with bilaterally placed single color μLEDs (Pig#3).
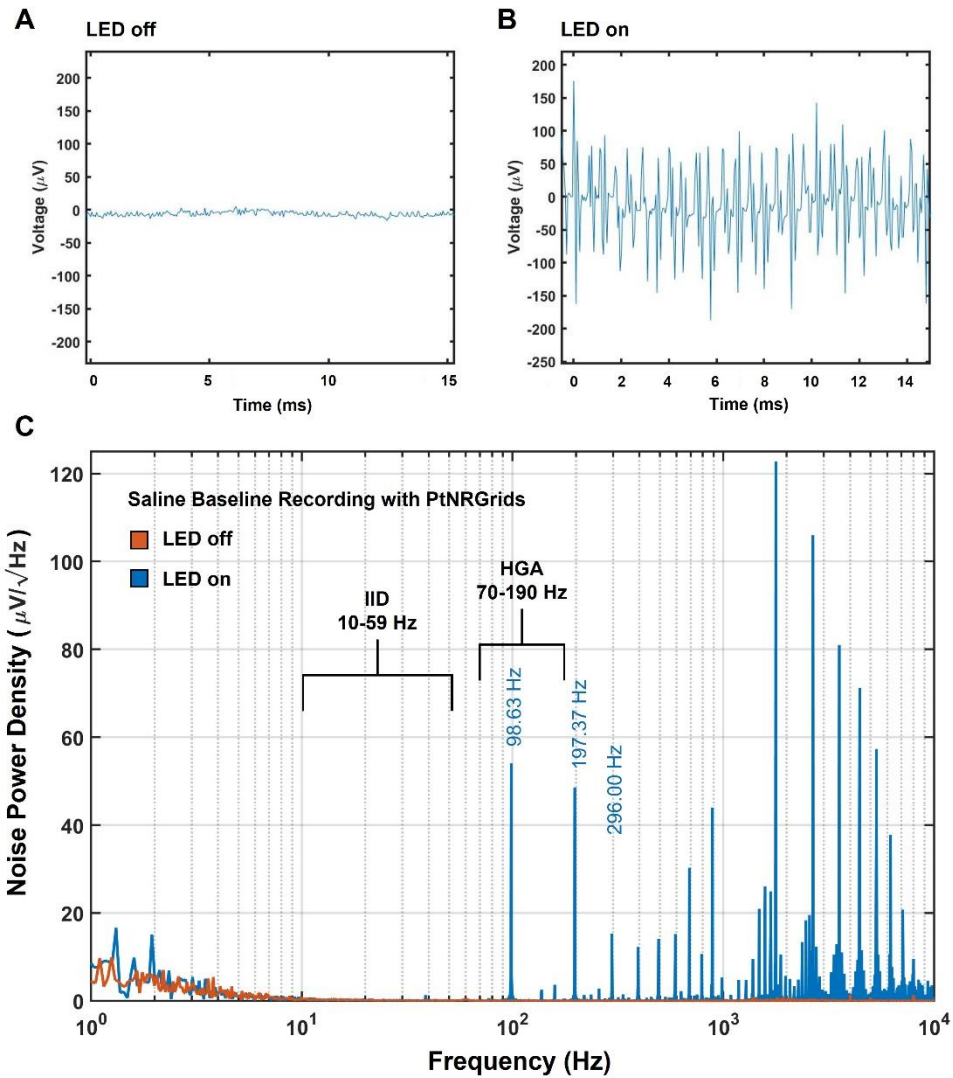
Figure S13. Electrical noise induced on μECoG by the μLED array operation. Raw waveform of μECoG grid recording baseline of saline with (A) LED powered off and (B) LED under operation. (C) Noise power density of μECoG signals with and without LED operation. The two main frequency windows, i) 10-59 Hz and ii) 70-190 Hz that we analyzed the data, are marked in the graph.
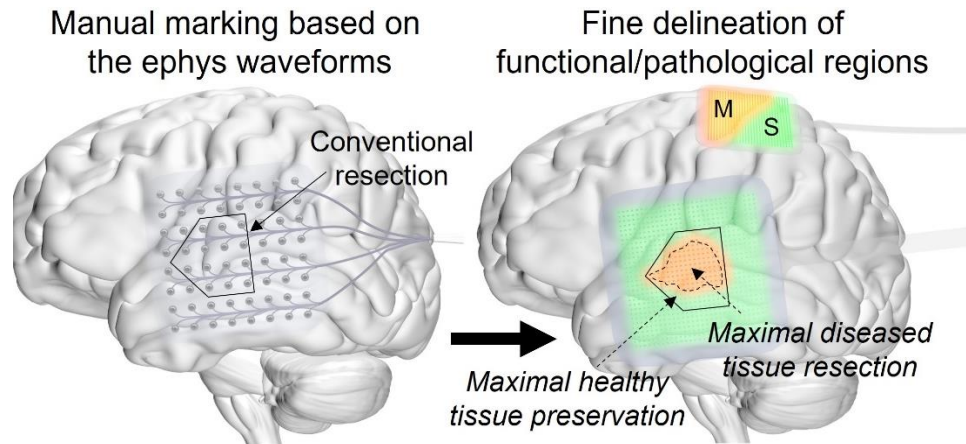
Figure S14. Illustration of the core concept of the iEEG-microdisplay that simultaneously measures and displays in real-time healthy and diseased brain regions and boundaries directly from the surgical field.

Table S1. Table summarizing pig models, anesthesia, type of device used, epileptogenic neurotoxin, and summary of recording.

Pig #	Date	Breed	Weight (kg)	Anesthesia	Anesthesia Maintenance	Type of iEEG-Microdisplay	Epileptogenic neurotoxin	Task
1	Sep. 21, 2022	Female Yorkshire	74	Midazolam 0.5 mg/kg Ketamine 10 mg/kg Atropine 0.004 mg/kg	Isoflurane and Propofol 8mg/kg/hr	32mm × 32mm, 1024 pixel	-	M1/S1 boundary, HGA mapping
2	Nov 15, 2022	Female Yorkshire	62	Midazolam 0.5 mg/kg Ketamine 10 mg/kg Atropine 0.004 mg/kg	Isoflurane and Propofol 8mg/kg/hr	32mm × 32mm, 1024 pixel	Pen-G	M1/S1 boundary, HGA mapping, Ojemann probe stimulation
3	Nov 16, 2022	Female Yorkshire	62	Midazolam 0.5 mg/kg Ketamine 10 mg/kg Atropine 0.004 mg/kg	Isoflurane and Propofol 8mg/kg/hr	32mm × 32mm, 1024 pixel	Pen-G	M1/S1 boundary, HGA mapping, IID mapping, Ojemann probe stimulation
4	Nov 18, 2022	Female Yorkshire	66	Midazolam 0.5 mg/kg Ketamine 10 mg/kg Atropine 0.004 mg/kg	Isoflurane and Propofol 8mg/kg/hr	32mm × 32mm, 1024 pixel	Pen-G	M1/S1 boundary, HGA mapping, IID mapping, Ojemann probe stimulation
5	Jan 12, 2023	Female Yorkshire	72	Midazolam 0.5 mg/kg Ketamine 10 mg/kg Atropine 0.004 mg/kg	Isoflurane and Propofol 8-10mg/kg/hr Vecuronium 5mg bolus	13mm × 32mm, 2048 pixel dual-color	4-AP	M1/S1 boundary, HGA mapping, IID mapping, Ojemann probe and sEEG stimulation

						2mg/hr IV				
6	Jan 13, 2023	Female Yorkshire	72	Midazolam 0.5 mg/kg Ketamine 10 mg/kg Atropine 0.004 mg/kg	Isoflurane and Propofol 8mg/kg/hr	13mm × 32mm, 2048 pixel dual-color	BIC			M1/S1 boundary, HGA mapping, IID mapping, Ojemann probe and sEEG stimulation

Table S2. Table summarizing rat models, anesthesia, type of device used, epileptogenic neurotoxin, and summary of recording.

Rat #	Date	Breed	Weight (g)	Anesthesia	Anesthesia Maintenance	Type of Brain EEG-Microdisplay	Epileptogenic neurotoxin	Task
1	April 18, 2022	Male Sprague Dawley Rats	500	Isoflurane 3-4%, transitioned to Ketamine/Xylazine	Ketamine/Xylazine (100 mg/kg ketamine / 10 mg/kg xylazine) re-dosed every 20-30 min	5mm × 5mm, 1024 pixel	4-AP	IID mapping
2	June 3, 2022	Male Sprague Dawley Rats	500	Isoflurane 3-4%, transitioned to Ketamine/Xylazine	Ketamine/Xylazine (100 mg/kg ketamine / 10 mg/kg xylazine) re-dosed every 20-30 min	5mm × 5mm, 1024 pixel	4-AP	Whisker barrel HGA mapping, IID mapping
3	June 9, 2022	Male Sprague Dawley Rats	500	Isoflurane 3-4%, transitioned to Ketamine/Xylazine	Ketamine/Xylazine (100 mg/kg ketamine / 10 mg/kg xylazine) re-dosed every 20-30 min	5mm × 5mm, 1024 pixel	-	Whisker barrel HGA mapping
4	Oct 31, 2022	Male Sprague Dawley Rats	500	Isoflurane 3-4%, transitioned to Ketamine/Xylazine	Ketamine/Xylazine (100 mg/kg ketamine / 10 mg/kg xylazine) re-dosed every 20-30 min	5mm × 5mm, 1024 pixel	BIC	Whisker barrel HGA mapping, IID mapping, Temperature rise monitor
5	Nov 7, 2022	Male Sprague Dawley Rats	500	Isoflurane 3-4%, transitioned to Ketamine/Xylazine	Ketamine/Xylazine (100 mg/kg ketamine / 10 mg/kg xylazine) re-dosed every 20-30 min	5mm × 5mm, 1024 pixel	-	Whisker barrel HGA mapping
6	Nov 9, 2022	Male Sprague Dawley Rats	500	Isoflurane 3-4%, transitioned to Ketamine/Xylazine	Ketamine/Xylazine (100 mg/kg ketamine / 10 mg/kg xylazine) re-dosed every 20-30 min	5mm × 5mm, 1024 pixel	BIC	IID mapping

Movie S1. Brain-iEEG microdisplay displaying the extent of the electrical field during cortical stimulation of the pig using Ojemann probe from 1 out of 2 pigs (Pigl #4).

Movie S2. Brain-iEEG microdisplay displaying the extent of the electrical field during cortical stimulation of the pig using sEEG probe from 1 out of 2 pigs (Pig #5).

Movie S3. Brain-iEEG microdisplay showing interictal discharge propagation in red color on pig brain together with the M1/S1 boundary displayed in green color.

Movie S4. High-resolution Brain-iEEG microdisplay showing interictal discharge propagation on the rat brain from 1 out of 2 rats (Rat #6).

Movie S5. Brain-iEEG microdisplay displaying the extent of the electrical field during cortical stimulation of the pig using Ojemann probe from 1 out of 2 pigs (Pig #3).

Movie S6. Brain-iEEG microdisplay displaying the extent of the electrical field during cortical stimulation of the pig using sEEG probe from 1 out of 2 pigs (Pig #6).

Movie S7. High-resolution Brain-iEEG microdisplay showing interictal discharge propagation on the rat brain from 1 out of 2 rats (Rat #4).